RICE UNIVERSITY

Novel Devices for Terahertz Wave Imaging, Wave-guiding and Sensing

by

Jingbo Liu

A THESIS SUBMITTED
IN PARTIAL FULFILLMENT OF THE
REQUIREMENTS FOR THE DEGREE

Doctor of Philosophy

APPROVED, THESIS COMMITTEE

Daniel Mittleman
Professor, Chair
Electrical and Computer Engineering

Junichiro Kono
Professor
Electrical and Computer Engineering
Physics and Astronomy

Kevin Kelly
Associate Professor
Electrical and Computer Engineering

HOUSTON, TEXAS
April 12, 2013

ABSTRACT

Novel Devices for Terahertz Wave Imaging, Wave-guiding and Sensing

by

Jingbo Liu

Several novel optical devices, which were designed to manipulate terahertz waves for broadband near-field imaging, wave-guiding (invisible space), and sensing (resonator), are presented in this thesis. We developed the original working concepts of each device, and demonstrated the prototype experimentally in our lab. The working concepts of physics were investigated in experiment, in simulation and in theoretical analysis.

We exploited a tapered parallel-plate waveguide (PPWG) as a novel probe for broadband near-field imaging. This imaging probe consists of two metal plates with the plate spacing gradually tapered from one end to the other. We proved that the space tapering enables this probe to propagate the broadband THz waves efficiently (with low-loss, no cut-off and nearly no dispersion) from the input end of large spacing into the narrow end of sub-wavelength spacing. Working in a reflection mode, this imaging probe is proved to be able to differentiate the dielectric features as well as topographic information on the sample. Combined with the methodology of filtered back projection, we reconstructed a two-dimensional image of a gold pattern on a GaAs chip by using this tapered PPWG probe. The smallest feature of ~100 μm is resolved by using the waves with average wavelength of 1.5 mm.

We studied the phenomenon of surface plasmon-polariton in THz range on the platform of a parallel-plate waveguide (PPWG). In this thesis, we show the characterization of the waveguide mode of a finite-width parallel plate waveguide by using an improved scattering-probe technique. An abrupt waveguide mode transition was observed at a very narrow frequency range. We demonstrated that this transition frequency is determined by the material properties of the waveguide, the frequencies of the electromagnetic waves as well as the geometry of the waveguide. This result provides a good guidance for the waveguide design for THz transmission.

We also exploited the capability of using the spoof surface plasmon to enhance the reflectivity of an interface between free space and a PPWG. We demonstrated that the reflection coefficient of this interface can be enhanced up to ~100 % at a designed frequency, by cutting a designed pattern of periodic rectangular groove on the output facet of the PPWG. A lateral shift and a phase shift of the reflected beam is observed in the experiment, which is a strong reminiscent of Goos-Hanchen shift. We carried out the experimental, simulation and theoretical characterizations of the lateral and phase shift. As an application, we designed and demonstrated a prototype of a band-pass THz resonator.

We introduced the concept of a waveguide-based two-dimensional inhomogeneous artificial dielectric into THz range. This artificial dielectric is the space between the two metal plates of a PPWG working in TE1 mode. We designed a THz mirage device (or an invisible space device) by using ray-tracing and full-wave

simulations, which contributed to the first experimental demonstration of such a device. A metal coin of size several times larger than the working wavelength can be hidden in the device without casting any shadow. This work is in collaboration with Dr. Rajind Mendis and the author of this thesis contributed to the design and characterization of the device in simulations.

Acknowledgments

I would like to express my gratitude to many people, whose generous help and encouragement make this thesis possible.

First of all, I want to thank my PhD adviser, Dr. Daniel Mittleman, for letting me join one of the best THz group in the world, and for guiding and supporting me through all the challenges in my PhD projects with his scientific excellence and continuous inspiration. Also I thank Dr. Rajind Mendis for his mentoring in my junior years, fruitful collaboration, and interesting and inspiring discussions on many aspects of research and life. I thank other members of my thesis committee, Dr. Kevin Kelly and Dr. Junichiro Kono, for their interests, advices, and precious time.

Special thanks should be given to the members of Mittleman's group, for their supports, interesting conversation, and friendships, which is an important part of the fun and enjoyment working in this group. Thanks to Dr. Hui Zhan, William Chan, and Jonathan Laib, for their good introductions and advices when I joined this group. I am also grateful to my office mates Dr. Victoria Astley, Dr. Marx Mbonye, and Daniel Nickel for their entertaining conversation and various assiatance in my research and life. Also I thank our new members, Kimberly Reichel, Nicholas Karl, Robert Mckinney, and Patrick Breen, for their various contributions to this thesis.

Last but not least, I owe a great amount of gratitude to my family, especially to my mother, for years of love, hard work and strong support that made my dream a reality.

Contents

List of Figures

Nomenclature

THz	Terahertz
THz-TDS	Terahertz Time Domain Spectroscopy
TX	Transmitter
RX	Receiver
SPPs	Surface Plasmon-Polaritons
SSPs	Spoof Surface Plasmons
PPWG	Parallel-Plate Waveguide
TEM	Transverse electromagnetic mode
TE	Transverse electric mode
ANSOM	Aperture-less near field Scanning Optical Microscope
FEM	Finite Element Method
FBP	Filtered Back Projection

Chapter 1

Introduction

1.1. Introduction

The terahertz wave is the electromagnetic radiation that covers the frequencies between 0.1 THz and 10 THz, which corresponds to wavelength from 30 μm to 3 mm. It was also called “THz Bridge” or “THz Gap” in the past, since it connects the frequency gap between microwave (millimeter-wave) and infrared radiations, where there was a lack of generation and detection methodologies. Although the THz wave is still less explored compared to the microwave and infrared field, the THz science and technologies have been growing rapidly in the past decades motivated by the curiosity of human being and the potential applications in various industries. In the THz community, which is a relatively young community, terahertz radiation is also called a sub-millimeter wave, T-ray, far-infrared, terahertz light, or THz.

Terahertz radiation was first exploited in Astronomical observations. In this field, the THz radiation is naturally generated as part of the black body radiation. It plays an important role for characterizing the cold 10-20 K dust in the interstellar medium in the Milky Way galaxy and in distant starburst galaxies. A number of observatories and telescopes were established around the world to monitor the radiation from the space in the THz range. Because of its high cost, low signal to noise ratio, and difficulties of daily operation, technologies for THz generation and detection were not applicable for many years, which hindered the exploration of the applications using this electromagnetic radiation. The THz technologies started to grow since 1965, when the first image generated by using THz radiation was demonstrated. Another dose of strong motivation was injected in 1995 [1], when the terahertz time-domain spectroscopy system was used to create THz images. Even now, Terahertz generation and detection is still in its infancy and remain in an area of active researches. As of 2013, there are a variety of terahertz generation and detection methodologies, such as the gyrotron[2], the backward wave oscillator[3], the far infrared laser [4], the quantum cascade laser[5], terahertz time-domain spectroscopy[6], and resonant tunneling diode (RTD)[7].

Along with development of the THz sources, the applications of THz technologies have been intensively investigated in many industries, benefitting from the marriage of technologies in microwave and optical frequencies. These applications usually involve using THz waves for imaging and spectroscopy. In medical imaging, a terahertz system provides a safe, non-invasive and painless diagnose tool for effective epithelia cancer detection[8], and a more accurate tool of

3D imaging for teeth inspection [9]. In the security inspection, the terahertz spectroscopy technique is employed to remotely detect drugs and explosives hidden in handbags or luggage, by making use of the unique “figure print” of these materials in THz spectrum[10]. In scientific research areas, the THz spectroscopy technique is a powerful analysis tool for providing information in chemistry, biochemistry, and material science [11]. The THz scanner provides historians a useful tool to see murals or paints through the coats of plaster, without harming these arts. In wireless communication industry, a new record of an extra-high rate (3 Gb/s) of wireless data transmission in a room was realized by using THz waves [12]. Because the THz frequencies lies in the middle ground of microwave and infrared in the spectrum, it is also widely investigated in order to understand the material response in this transition frequency [13], and to prove some novel concepts which were not applicable in the other frequencies [14-17].

In the development of science and technologies for THz imaging and spectroscopy, there were some challenges with the THz radiation, which limit the applications of THz technologies in the real-world environment. For example, the wave vapor has very strong rotation transition in THz range, which results in intense absorption bands. And water vapor is one of the major contents of the ordinary air in the atmosphere. Therefore the earth’s atmosphere is a natural absorber of terahertz waves, which prevents terahertz wave from applications such as long distance (> 500m) wireless communications, and also adds undesired water absorption lines in the spectroscopic characterization of materials. Another example of the challenges is the lack of an efficient waveguide, which transmit the broad-

band terahertz wave to the area of application without excessive loss of information or signal degradation.

1.2. The scope of this thesis

The motivation of my doctoral research is to develop novel devices and systems with improved performance for THz imaging, wave-guiding and sensing. In this thesis, I have included all research projects accomplished as my PhD works, either in cooperation with other authors or completed independently.

For a better understanding of this thesis, I have included the necessary background for each project, along with an introduction to the THz-TDS system (Chapter 2). The first project of my doctoral thesis was for a THz spectral near-field imaging technique that exploits a novel imaging probe (in Chapter 3). In the second project (the first part of Chapter 4), I characterized the waveguide mode of a finite-width parallel plate waveguide in both experiment and simulation, which shows an abrupt mode transition from plasmonic mode to the traditional TEM mode. In the third project (the second part of Chapter 4), I discovered a new physical phenomenon, which explores the concept of using spoof surface plasmons (SSPs) to enhance the reflectivity at the output facet of a parallel plate waveguide. As a step forward, I applied this new concept into a novel THz band-pass resonator and demonstrated a prototype of the resonator in the experiment. For my last project (Chapter 5), I designed a THz mirage device by using both the full-wave simulations based on the finite element method and the simulations based on ray-tracing, which

exploits a parallel-plate waveguide working in TE1 mode as a two-dimensional inhomogeneous artificial dielectric. This design contributes to the first experimental demonstration of such a device.

Interestingly there is a common link for all my doctoral research projects, which is a parallel-plate waveguide (PPWG). This simple classic textbook structure of waveguide has supreme qualities as a waveguide for broad-band THz wave propagation[18, 19], and it has been the platform for various applications of THz technologies. The lowest fundamental waveguide modes of a PPWG are transverse electromagnetic mode (TEM mode) and the first order of transverse electric mode (TE1 mode). The imaging probe for the THz near-field imaging project is a spacing-tapered parallel plate waveguide working in TEM mode. In the project of waveguide mode characterization, the finite width parallel-plate waveguide is a variation of the traditional infinite width PPWG. The waveguide for SSPs enhanced reflectivity at the output facet is a parallel plate waveguide working in TEM mode. The concept of the two-dimensional inhomogeneous artificial dielectric for the last project is based on the effective refractive index of a PPWG working in TE1 mode.

Chapter 2

Background

2.1. Terahertz Time-Domain Spectroscopy

Terahertz time-domain spectroscopy (THz-TDS) is a powerful tool widely used in the terahertz community. Basically it consists of an ultrafast laser, an optical delay line, a THz transmitter and a THz receiver. In this technique, the electric field of the radiation is measured in the time-domain, and then the time-domain waveform yields both the amplitude and the phase of the radiation in frequency domain through Fourier transformation. For the THz transmitter, there are two different ways to generate THz waveform in the THz-TDS system: optical rectification and photoconductive switch (photoconductive antenna). The optical rectification method has a broader band-width in the spectrum while the photoconductive antenna gives a better signal-to-noise ratio (SNR). For the THz receiver, there are also two different methods to detect THz radiations: electro-optic

sampling, which is the inverse of the second-order non-linear phenomenon working for optical rectification, and the photoconductive switch. In the scope of this thesis, we only use the THz-TDS systems that have photoconductive switches for both THz wave generation and detection.

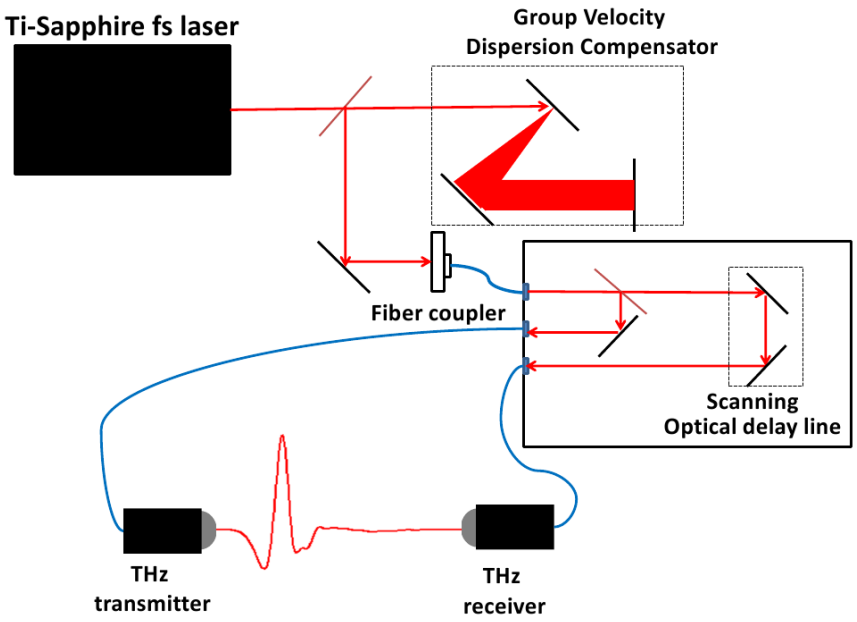

Figure 2.1 Schematic of a fiber-coupled THz-TDS system

The diagram of a typical fiber-coupled THz-TDS system is shown in figure 2.1. The Ti:Sapphire femtosecond laser generates a series of ultrafast pulses, which have a duration of ~100 femtosecond and center wavelength of 800 nm working at a repetition rate of 80 MHz. The ultrafast pulse first goes through a grating group velocity compensator, which pre-compensates for the group velocity dispersion that the THz pulse suffers from the propagation in optical fibers in later stage. The free space laser pulse is then coupled into an optical fiber, which is connected to the

THz-TDS controller unit. The power conversion rate from the free space wave into the wave in the optical fiber is less than 50%. In the THz-TDS controller unit, the laser beam is split in two: one goes straight to the transmitter head, which contains a photoconductive switch for THz generation; the other part is guided into a fast free-space scanning optical delay line, which provides a time-delay between the gating femtosecond laser pulse and the THz wave, and then goes into the receiver head. Since both the transmitter and receiver heads are fiber-coupled, they can be conveniently moved without changing the optical set-up. A typical THz radiation obtained from a commercialized fiber-coupled THz-TDS system is shown in figure 2.2. This is the THz source for all the experimental work described in this thesis.

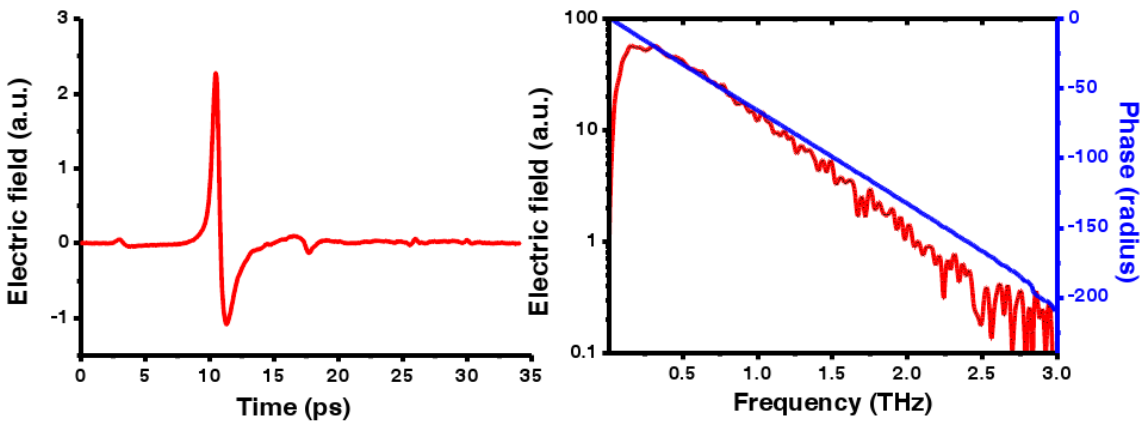

Figure 2.2 A typical THz waveform obtained from a THz-TDS system. The electric field of the THz radiation is measured on time domain (left). The spectral electric field amplitude and phase of the THz pulse is extracted from a fast Fourier transform (right).

2.2. Terahertz Near-Field Imaging

The terahertz radiation has a number of unique characteristics, making it a good candidate for a lot of applications in imaging and sensing. For example, most polar molecules in the gas phase have very sharp absorption lines (called finger prints) in the THz range, resulting from the unique rotational or ro-vibrational spectra of the absorbing species [20]. THz waves penetrate most dry, nonmetallic and nonpolar substances, such as plastic and cardboard, and also collect spectroscopic information of the contents inside an opaque box. In addition a wide range of explosives have unique spectral information in the THz region [21]. Due to these properties, the THz wave is good for package scanning, quality control and security inspection. Therefore this method of using terahertz radiation for imaging and sensing has been one of the most active research areas in the THz community for many years [20, 22, 23]. A recent comprehensive review of the advances in THz imaging can be found in a publication from Mittleman Group [23].

The THz imaging techniques using far-field method have a wavelength-related limit on resolution. According to Abbe's law, the far-field microscopy has a resolution limit because of the diffraction nature of propagating electromagnetic waves. The minimum length that can be resolved in the image is expressed in the formula as below:

$$d = \frac{\lambda}{2NA} \qquad (2.1)$$

where d is the resolution, λ is the wavelength and NA is the numerical aperture of the imaging optics. For a typical THz radiation, the wavelength is 0.3 mm at frequency 1 THz, and even longer for the radiation at lower frequencies. This diffraction-based resolution limit constrains the ability of THz imaging to resolve small features bellow the wavelength, the details of such features are of more interests in some studies.

To overcome this limit, a variety of aperture-based and aperture-less near-field (evanescent field) microscopy techniques have been introduced into the THz imaging community since the first demonstration in 1998 [24, 25]. The challenges in near-field imaging are that the evanescent waves, which contain information on a sub-wavelength scale, are strongly localized on the sample surface and do not propagate into the free space. In the near-field technologies, the evanescent field information of the imaging object is collected and used to make images by various methodologies. Most of them involve a disturbance of the evanescent wave. This disturbance helps couple the near-field waves into freely propagating waves or the waves propagating in a waveguide (aperture), which are then collected at a THz receiver. Since the measured signals contain the near-field information, these near-field techniques improve the resolution significantly.

One category of THz near-field imaging techniques is aperture-based. In this technique a sub-wavelength aperture is held close to the imaging sample for illumination or for signal collections. The first aperture for THz near-field imaging was a tapered conical metal tip, with a sub-wavelength opening at the narrow

end[24]. This probe could be raster-scanned across a planar object with an imaging resolution determined by the size of the aperture as well as the distance between the aperture and the imaging object. However there are two undesired effects with this aperture-based near-field imaging technique. One is that the power transmission through the sub-wavelength aperture is usually very small, with a transmission coefficient decreasing approximately as the sixth power of the aperture size [26, 27]. For example, reduction of one magnitude on aperture diameter, which improves imaging resolution of only a magnitude, causes a loss of six magnitudes in signal to noise ratio. The other effect is the waveguide effect of the aperture. Since the aperture is essentially a waveguide, it has a cut-off frequency that is roughly inversely proportional to its cross-sectional size. For the waves of frequencies below the cut-off, the omega loss of the aperture is so overwhelming that nearly no signal can be detected. Thus this poses a limit on aperture size for the imaging using waves at a fixed frequency. Below this limit the signal of interest is cut off. Another challenge that is unique to the imaging technique using broad-band THz waves is the associated strong dispersion [24, 28, 29]. If the aperture has a cut-off close to the frequency spectrum of the pulsed signal, the transmitted signal suffers from a strong dispersion and becomes chirped with a long tail after the main pulse. Weighing all these factors, the resolution of the aperture-based near-field technique is usually very difficult to exceed a twentieth of operating wavelength [30, 31].

An alternative near-field imaging technique is aperture-less scanning optical microscopy (ANSOM), which was first developed in optical and infrared regions in

the 1990s and was implemented in THz range in the 2000s[32, 33]. In a typical THz ANSOM experiment, a metal probe with a sharp tip is held close to the imaging object and an incident THz beam is focused onto the area between the probe tip and the sample. A few groups have reported different methods to collect the near-field signals [32-35]. In one method the metal probe is connected to a piezoelectric transducer being modulated at a frequency. The vibration of the probe is in a direction normal to the sample surface. This vibration of the micron scale introduces a spatial modulation to the scattered electromagnetic wave under the metal tip. The piezoelectric transducer is driven by an AC signal at a fixed frequency, which is then used as a reference to amplify the scattered waves [33-35]. A near-field image of nanometer resolution has been demonstrated that utilizes this ANSOM method [33].

As a part of my PhD thesis, I introduced a novel near-field imaging probe which is based on a spacing-tapered parallel-plate waveguide. This probe doesn't have the undesired effects that commonly come with the aperture-based near-field imaging techniques, such as the undesired dispersion and high propagation loss. I demonstrated the two-dimensional imaging ability of the novel probe by combining it with a filtered-back-projection method. A feature of ~100 μm is resolved in the image by using a THz wave of an average wavelength of 1.5 mm.

2.3. Terahertz Surface Plasmon-Polaritons (SPPs)

Collective electric charge oscillations at the interface between an insulating dielectric medium and a conductive medium are known as surface plasmon-polaritons (SPPs) or surface waves. For example, in 1907 Zenneck reported the propagation of radio waves on the surface of the earth [36]. Surface waves are usually excited by electromagnetic waves and propagate on the interface between the two mediums in a wave form. Generally, the surface plasmon-polariton has an effective wave vector (k_{sp}) larger than the wave vector of electromagnetic waves at the same frequency in the vacuum (k_0). Thus the wave vector normal to the metal surface ($\sqrt{k_0 - k_{sp}}$) is imaginary, which makes an energy confinement of surface waves on the interface. The strength of this confinement depends on the difference between k_{sp} and k_0. Theoretically the wave vector of surface waves mostly depends on the response of the conductive mediums to the interacting electromagnetic waves. For most common metals, such as aluminum and gold, the surface wave vector (k_{sp}) shows significant difference from the wave vector in free space (k_0) at frequencies of the visible range. In the last two decades, SPPs in the infrared to the visible light range have been intensively studied, inspired by suprising phenomenon of the extrodinary transmission through subwavelength apertures on a metal sheet [37-39].

At terahertz frequencies, due to the relatively weak electromagnetic response of the metal [40, 41], surface waves are loosely bounded to the metal-dielectric (air) interface. Thus the effective wave vector (k_{sp}) of the surface waves

parallel to the metal-dielectric interface is almost the same as that of the free propagating electromagnetic waves (k_0), which makes it difficult to differentiate the bounded surface plasmon-polaritons and free propagating electromagnetic waves parallel to the metal-dielectric surface.

A simple context of a surface plasmon polariton is the surface wave propagating on a planar interface between air and metal [42-45]. The in-plane wave vector of the SPPs on a planar interface is expressed as

$$\beta(\omega) = k_0\sqrt{\varepsilon_d\varepsilon_m(\omega)/(\varepsilon_d + \varepsilon_m(\omega))} \qquad (2.2)$$

Where ε_d and $\varepsilon_m(\omega)$ are the complex permittivities of the dielectric and metal respectively, k_0 is the wave vector in vacuum. The dielectric ε_d is weakly dependent on frequency ω for most dielectrics, such as the air of ε_0. However the metallic ε_m is strongly dispersive for most metals or conductive dielectrics. When ε_m is much larger than ε_d, the wave vector of surface waves is $\beta(\omega) \approx k_0\sqrt{\varepsilon_d}$, approximating to the dispersion relation of freely propagating electromagnetic waves in the dielectric. At a frequency when ε_m is a complex number with negative real-part and the amplitude of real-part is equal to ε_d, $\beta(\omega)$ reaches it maximum. The surface waves at this frequency become very lossy and stop to propagate on the metal-dielectric interface. The frequency at which $\beta(\omega)$ reaches maximum is called an asymptotic SPP frequency.

The asymptotic SPP frequency is intrinsically defined by the dispersion curve of the metal. We used a simplified Drude model to approximately describe metal permittivity as below:

$$\varepsilon_m = 1 - \frac{\omega_p^2}{\omega^2} \tag{2.3}$$

where $\omega_p = \sqrt{Ne^2 / (\varepsilon_0 m^*)}$ is the bulk plasma frequency of the meal, e is the electron charge, N is the density of electrons on the metal surface, and m^* is the effective mass of the electrons. When electromagnetic wave frequency becomes $\omega_p / \sqrt{2}$, the permittivity of the metal at this frequency is -1, and the permittivity of the air is +1, the wave vector of the surface wave reaches maximum. Thus the asymptotic frequency of the surface waves on the metal-air interface is $\omega_p / \sqrt{2}$. For common metals, such as Al, Au, Ag, their asymptotic frequency for air-metal interface is located in the visible and ultraviolet range. At Terahertz frequencies, the dispersion relation of SPP is close to dispersion curve in free space, or called light line, and the effective wavelength on the plane is approximate to the free space wavelength. Thus the SPP at THz is poorly confined on the surface, and are called Sommerfeld or Zenneck waves [36, 46].

2.4. TE1 Mode in a Parallel-Plate Waveguide and a Two-dimensional artificial dielectric

The parallel-plate waveguide (PPWG) that works in the fundamental mode (TEM mode) has been investigated as a platform for many fundamental and applied researches. It has excellent waveguide properties for propagating the broad-band THz waves with low-loss, no-cut-off and nearly no-dispersion [17, 19, 47-50]. Because of the undesired cut-off frequency, the high order waveguide modes of PPWG (TE1 or TM1) have not been studied for practical applications until very recently [15-17, 51-54]. A PPWG working in higher modes has a strong propagation loss and a strong dispersion for the single pulse, due to its cut-off frequency. Recent interests in the first transverse-electric (TE1) mode of a PPWG were inspired by its potential use for an extra-low loss, low-dispersion and low-diffraction waveguide for the THz radiations [15, 16, 53-55]. Compared to the other waveguides, this novel waveguide was theoretically expected to have a loss as low as a few dB/km, which is a world record of the THz waveguides [16].

Basically, a parallel plate waveguide working in the TE1 mode has a cut-off frequency expressed as bellow[18]:

$$f_c = \frac{c}{2b} \tag{2.4}$$

where c is the speed of light in vacuum, b is the plate spacing of the PPWG. The phase velocity of the propagating waves in the TE1 mode can be expressed by the formula bellow:

$$V_p = \frac{c}{\sqrt{1-(\frac{f_c}{f})^2}} \tag{2.5}$$

where f is the frequency of the electromagnetic waves.

The concept of a two-dimensional artificial dielectric was exploited in this thesis. Basically this concept relays on the fundamental definition of the refractive index: the effective index of refraction in a medium is equal to the ratio of the speed of light in vacuum (c) to the phase velocity (V_p) of the electromagnetic wave in the medium. When the parallel-plate waveguide works in the TE1 mode, the space between the two metal plates has an effective refractive index defined by the equation below:

$$n = \frac{c}{V_p} = \sqrt{1-(\frac{f_c}{f})^2} \tag{2.6}$$

When the parallel-plate waveguide works in the TE1 mode, the space sandwiched by the two metal plates becomes an artificial medium with refractive index varying between a value close to unity and zero. This concept has been previously demonstrated in the terahertz frequencies by a series of experiments, which were designed to achieve some classical optical phenomenon, such as the total internal reflection, the Brewster's effect and the convergent PPWG-lens [15,

54, 56]. Although this is a new concept in the THz community, similar concepts at microwave frequencies have been investigated half a century ago [57-61].

In this thesis, we investigated this concept by engineering the index of refraction between the two metal plates in order to manipulate the electromagnetic wave propagation. By substituting the cut-off frequency $f_c = \frac{c}{2b}$ into (2.6), the effective index of refraction is calculated as:

$$n = \sqrt{1 - (\frac{c}{2bf})^2} \tag{2.7}$$

For a fixed frequency, the index of refraction in the 2-D artificial medium can be engineered by changing the separation b between the two metal plates. This engineer-able 2-D inhomogeneous artificial dielectric offers a new approach to achieve a 2-D matamaterial, and opens up the possibilities to control the flows of electromagnetic waves in counter-intuitive ways[62].

I showed the collaborated work with Dr. Rajind Mendis on demonstrating the application of the 2-D artificial medium to implement a THz mirage device. The mirage device was designed by the author of this thesis using the ray tracing simulation and the 3D full-wave FEM simulation [63], and was demonstrated in experiment by Dr. Rajind Mendis.

Chapter 3

Terahertz Wave Broadband Near-field Imaging

3.1. Background

There have been continuous interests in terahertz near-field imaging in the past decade, motivated by development of THz time-domain spectroscopy technique [20, 24]. The spectral window of THz-TDS covers the range from 0.1 THz to 10 THz, which is rich of spectral information. One of the challenges of near-field imaging using broad-band THz waves include the resolution limit due to the wave diffraction, which is usually in millimeter scale. To overcome this diffraction-based resolution limit, a variety of aperture-based and aperture-less near-field imaging techniques have been developed [24, 32, 64, 65]. These aperture-based and aperture-less imaging probe can successfully reduce the resolution down to nanoscale [33].

For the aperture-based imaging technique, as the imaging probe reduces the tip size, the propagation loss in the probe increases exponentially. Also the pulsed THz wave suffers from a strong chirping effect, due to the dispersion associated with the cut-off of the probe. These undesired effects continue to pose significant challenges to the near-field techniques for broadband THz imaging [23].

The PPWG has been an excellent platform for many THz applications in the last decade, for its incomparable properties as a waveguide which has low-loss non-cut-off and low-dispersion [19, 66-69]. Recently, a PPWG with small plate spacing was used as a line-illumination probe for broad-band THz near-field imaging [49]. In that work, the transmission signals through the waveguide were used as a line illuminator and the signals passed through sample were collected by a single receiver. Then all the collected signals were used to reconstruct a sub-wavelength image based on a filtered back-projection algorithm. However, the reflection loss at the output aperture of the PPWG is dominant according to the recent study on the reflection coefficient from the output facet of a PPWG [55].

A more recent technique that utilizes a tapered parallel-plate waveguide (PPWG) for delivering broadband THz pulses into a sub-wavelength scale has been studied both theoretically [70] and experimentally [71, 72]. In this technique the plate spacing of a PPWG is tapered from a large size at the input into a sub-wavelength size at the output. To minimize the reflection loss in the tapering process, the slope of the spacing change is kept small and smooth. This tapered PPWG has an advantage of efficiently quasi-optically coupling the free space broad-

band THz waves into the waveguide. The coupled waves are then delivered to a sub-wavelength aperture [19, 73, 74]. In this chapter, I investigated the tapered parallel-plate waveguide (PPWG) as a candidate for an imaging probe (Fig 3.1), which overcomes the resolution limit, the strong propagation loss, and undesired dispersions for near-field imaging.

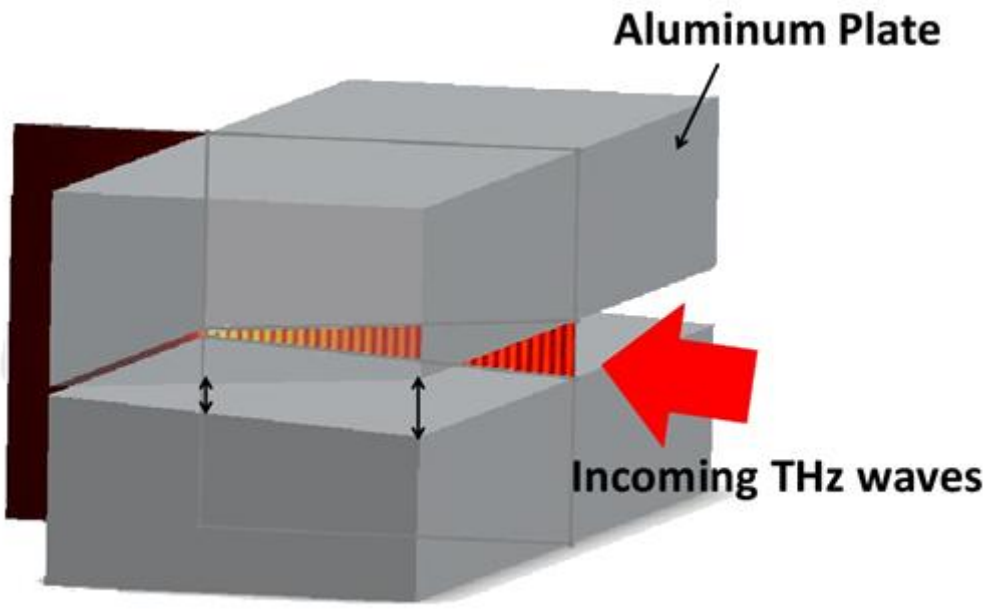

Figure 3.1 – Schematic of a tapered-parallel-plates probe (the front facet of the top plate is set as transparent). The cross-section shows simulated electric field distribution in the tapered PPWG (FEM).

We use the reflected wave for imaging, because there is a conflict between a good imaging resolution and a good signal-to-noise ratio by using the transmissions. For a parallel-plate-waveguide, the impedance mismatch between the characteristic impedance of the waveguide and that in the free space increases as the plate spacing

decreases, resulting to a decreased transmission. For a rough approximation, the amplitude of the transmitted radiation decreases approximately as the ratio b/λ, where b is the plate spacing [75]. Thus for a better resolution, a PPWG of a smaller the plate spacing should be used, which then puts more loss on the transmission signal. Using the reflected wave, rather than relying on the transmitted wave, permits us to avoid the concerns associated with large reflection due to the wave impedance mismatch, and therefore achieve better spatial resolution and an improved signal-to-noise (S/N) ratio. Similar techniques have been demonstrated at millimeter wave frequencies [76, 77].

3.2. Filtered Back Projection

In this section I give a brief introduction to the filtered back projection method, which is a matured methodology widely used in medical imaging. The essential step in the filtered back projection is a Radon transform, which is named after the Austrian mathematician Johann Radon [78]. Basically the Radon transform is the integral transform consisting of the integral of a function over straight lines. Let $f(x, y)$ be a continuous function vanishing outside a large area in Euclidean plane $\mathbf{R}^2$, where $f(x, y)$ could be a density function of a target patient, or the grey scale of an image. The Radon transform is a function defined on a set of straight lines L in $\mathbf{R}^2$ by the line integral along each line,

$$Radon(f) = \int_L f(x, y) dL \tag{3.1}$$

The straight line L can be described by two parameters, α and s, where s is the distance between line L and the origin point, and α is the angle the normal vector to L makes with x axis. Thus Radon transform can be expressed by the two parameters as:

$$Radon(f)(s,\alpha) = \int_{-\infty}^{\infty} f((t\sin\alpha + s\cos\alpha),(-t\cos\alpha + s\sin\alpha))dt \qquad (3.2)$$

where t is a length on the integral line.

The Radon transform of an image can be plotted as a function of s and α, which is often called sonogram. The name originates from a fact that the Radon transform of a Dirac delta function is a sine wave on the graph. In the imaging process, such as that in Computerized Tomography techniques [79], the radon transform is usually applied in an inverse way. Because the measured signals, which would then be used as the input to the transform, are the line integrals of the sample image according to the instrument settings. To reconstruct the original image ($f(x,y)$) from the measured signals, an inverse radon transform is usually performed. Explicit and computationally efficient inversion formulas for the Radon transform and its dual are available [78, 79]. In our study, we used the build-in function in MATLAB for inverse radon transform. The syntax in MATLAB is as:

$$I = iradon(R,\alpha) \qquad (3.3)$$

where I is a matrix for the reconstructed image, R is a matrix corresponding to the Radon transform of the sample image. Columns of R represent *s* while rows of R

represents α, as shown in (3.2). Advanced parameters of this function can be found in the help file in MATLAB.

3.3. Imaging With A Tapered Parallel-Plate Waveguide Probe

The experimental set-up consists of a THz-TDS system, with the fiber-coupled transmitter and receiver positioned as shown in Fig 3.2. The transmitter and receiver are situated close to the focal plane of a Teflon lens that has a focal length of 6 cm. The tilt angle between the transmitter and receiver is 10°. An aluminum-foil shield is located between the transmitter and receiver to block any interference between them. In order to excite the TEM mode in the PPWG, the input THz waves are polarized perpendicular to the waveguide plates. A plano-cylindrical Teflon lens of 1.2 cm radius and 4 cm length is used to couple the incident THz waves into the waveguide and also couple the reflected waves out of the waveguide. The PPWG has a width of 5 cm and a spacing tapered from a large size (~ 1.5 – 2 mm) at the input facet to a much smaller size (~ 20 – 100 μm) at the output facet, within a propagation length of 2.5 cm. This tapered PPWG transfers the broad-band waves into the sub-wavelength output facet, so that it can serve as a near-filed probe with the resolution determined by the output spacing size [49, 71, 72]. The imaging sample mounted on the rotation stage is placed in a close proximity (down to ~ 20 μm) to the output facet of the waveguide. The two motion-control stages are used to scan the sample position relative to the waveguide. The measured data are then used to reconstruct the images by the filtered-back-projection algorithm. [49, 78]

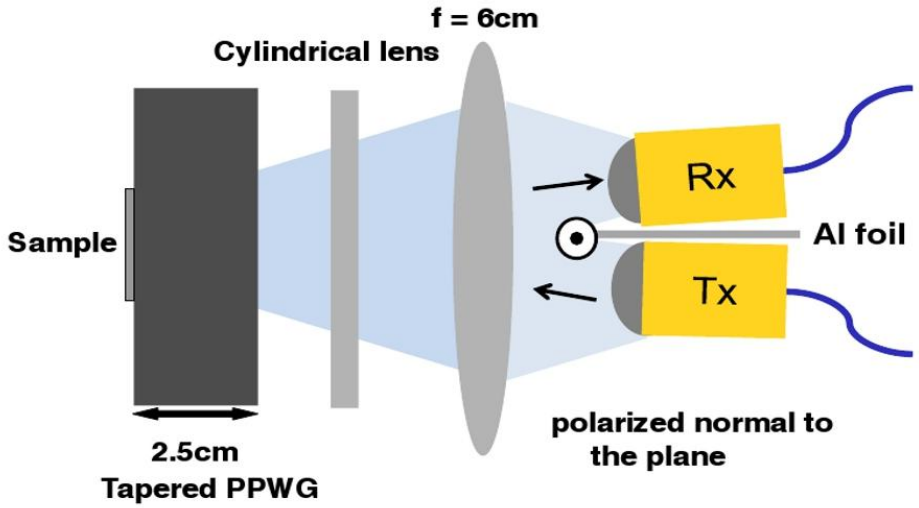

Figure 3.2 –Schematic of experimental set-up

In order to investigate the imaging capability of the probe working in a reflection mode, we characterized the reflected signals from the output aperture of PPWGs in different geometries. The sub-wavelength aperture at the output facet results in an impedance mismatch between the characteristic impedance of the waveguide and that in the free space. This leads to a reflection of the propagated signal back into the waveguide [75, 80, 81]. We measured the reflected signal from the output facet for three cases: a PPWG with a spacing of 2 mm, the same PPWG with a mirror closely attached to the output facet, and a PPWG with the plate separation tapered from 2 mm at the input to 200 μm. For the untapered PPWG without the mirror, the reflection is nearly zeros as expected. We note that the broadband reflection from the tapered PPWG (solid line in Fig 3.3(a)) is comparable in amplitude to the reflection from the mirror at the end of the untapered PPWG

(dashed line in Fig 3.3 (a)). Thus, this tapered PPWG probe reflects most of the input signal, making it feasible to work in reflection mode. We also note that there is some low-pass filtering in the reflected signal caused by the impedance mismatch, which can be readily understood by the b/λ throughput that we mentioned in section 3.1. Furthermore, the fact that these two signals are comparable is a good indication of the higher S/N ratio that is achievable in the reflection geometry compared to a transmission one, at these small output plate separations.

Then we characterize the effect of a flat object (made of glass, silicon, or aluminum) situated at the waveguide output. We taper the PPWG spacing from 1.5mm to 20 μm and consider the change in the reflection coefficient induced by an object placed in close proximity (~20 μm) to the output facet. Due to the higher refractive index compared to air, this object modifies the impedance mismatch and leads to a change in the reflection. This change in the reflection depends on the distance from the object to the output facet, as shown in Fig. 3.3 (b). We note that in our experiment, it is not possible to have the object exactly in contact with the very edge of the probe due to practical considerations. The closest possible distance between the object (substrate) and the output facet of the tapered PPWG is ~ 20 μm. Counter intuitively, at this distance, we do not observe a perfect mirror-reflection from the aluminum object. This is better understood via numerical simulations of the physical problem using the finite-element method [63]. These results (Fig. 3.3 (c)) reproduce our measurements qualitatively, indicating a turning point in the curve as the object is brought closer. To understand this further, we could imagine that when the object is 20 μm away from the output facet, it forms a waveguide T-

junction with the 20 μm plate spacing at the output facet. This could help to guide energy out of the waveguide along the output facet, leading to the observed drop in the amplitude of the reflected signal. We note that in our simulation, when the aluminum object is in perfect contact with the output facet, there is an almost 100% reflection, as expected.

When the object is moved further away from the output facet, there are fewer disturbances to the near field, and a much stronger reflection results. The reflection keeps increasing until the distance is about 0.1mm and results in a relatively stable reflection beyond this point. Based on this result, a topographic feature on a sample of height 0.1mm or less could be identified by the change in the reflection. This change is due to the disturbance to the waves in the near field, which extends from the end of the waveguide to a distance roughly equal to the waveguide gap [80]. We also note that in both Figs. 3.3 (b) and 3.3 (c), at any particular distance within the transient regime, the reflected signal differs for different substrate materials. Therefore, the tapered-PPWG probe in reflection mode is able to differentiate both topographic features and dielectric properties of the sample.

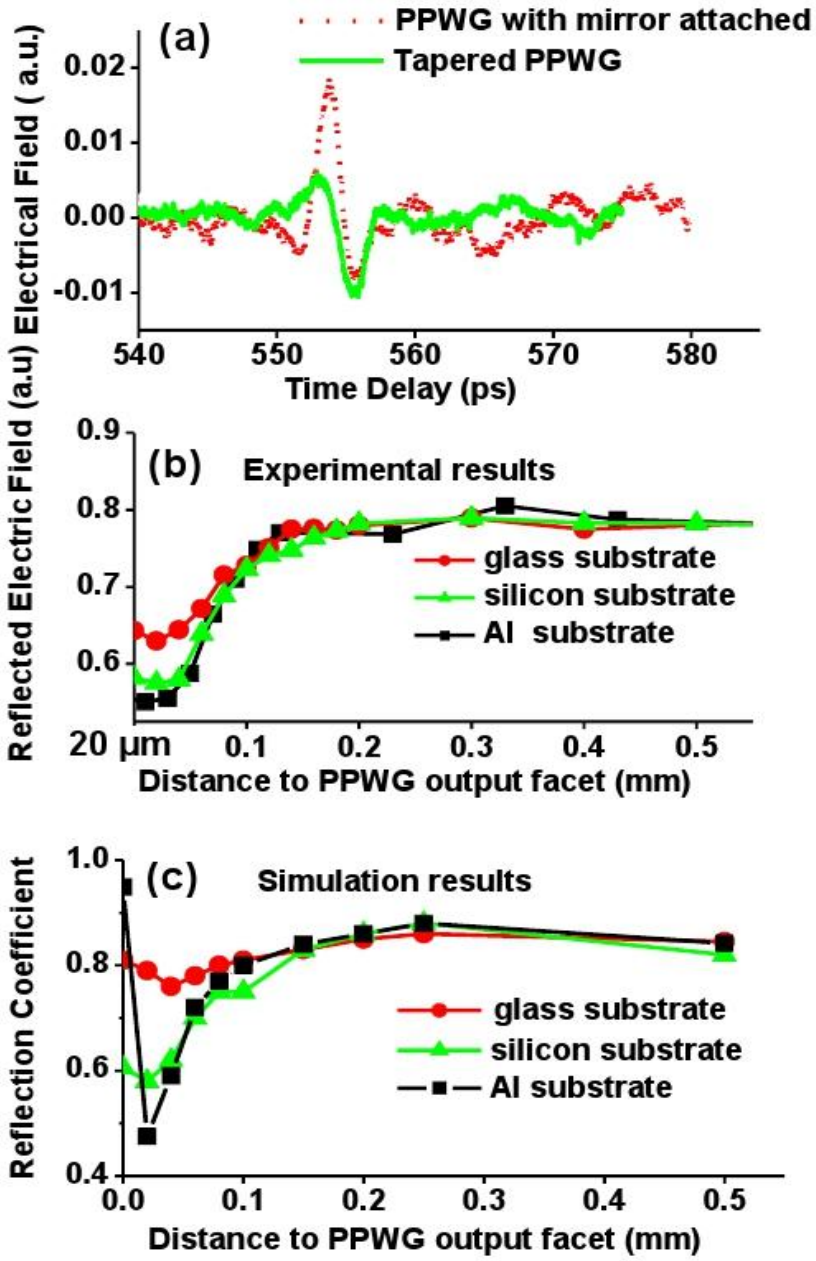

Figure 3.3 (a) Time-domain reflections from an untapered PPWG of plate spacing 2mm with attached mirror and from a PPWG with tapered plate spacing, from 2mm to 200 lm. (b) Measured reflected electric field as a function of sample distance to the waveguide output facet, for glass, silicon, and aluminum (flat) samples. (c) Simulated reflection coefficients corresponding to the configurations in (b).

To further investigate the imaging capabilities, we used a sample consisting of a gold pattern on a GaAs substrate, as shown in Fig. 3.6 (a). This sample is essentially flat (within ~ 100 nm), so no topographic information is retrieved. However, we show that it is possible to obtain information based on the dielectric contrast. We scan the sample across the output facet of the tapered PPWG in a direction normal to the plates (x direction in Fig. 3.4). The spacing at the output facet of the tapered-PPWG probe and its proximity to the sample determine the best resolution this imaging technique can achieve[23]. This tapered PPWG gives high resolution only in one direction: the direction normal to the plates. To obtain a two dimensionally resolved image, a linear scan (x-scan) alternating with a rotational scan (Fig 3.4) of the sample was carried out based on the filtered-back-projection (FBP) approach, as discussed in last section. The maximum length on the sample is ~ 4.5 mm, so the linear scan range is set as from 0 mm to 9 mm with a step of 20 μm, to make sure the complete sample area is covered. The rotation is around the optical axis of the input beam, covering a range from 0° to 175° with a step of 5°. In total, 16,236 projection time-domain signals were recorded, and each signal has frequency components ranging between 0.01 THz to 0.9 THz. To improve the S/N ratio, each projection signal was averaged over 10 iterations. Fig 3.5 (a) shows a surface plot of one set of typical time-domain signals in one linear scan at the angle of 0°. We observe that as the imaging sample is scanned across the probe, there is a valley of the time-domain amplitude along the linear scan direction, which reflects the dielectric information on the sample. The tiny variation of the signal amplitudes represents the features of the good pattern on the sample. The time-domain signals

are Fourier transformed, and the spectral information is extracted for image processing. Fig 3.5 (b) gives an example of the sinogram for the imaging sample, the signal amplitude of which is extracted from the spectrum at frequency of 0.3 THz. In order to further improve the S/N ratio, we use the integral of the spectral amplitude over a range of frequencies to reconstruct the image [78]. The chosen spectral range was from 0.05 THz to 0.5 THz (λ ~ 0.6–6 mm). Thus the spectrally weighted mean wavelength used for image reconstruction is 1.5 mm.

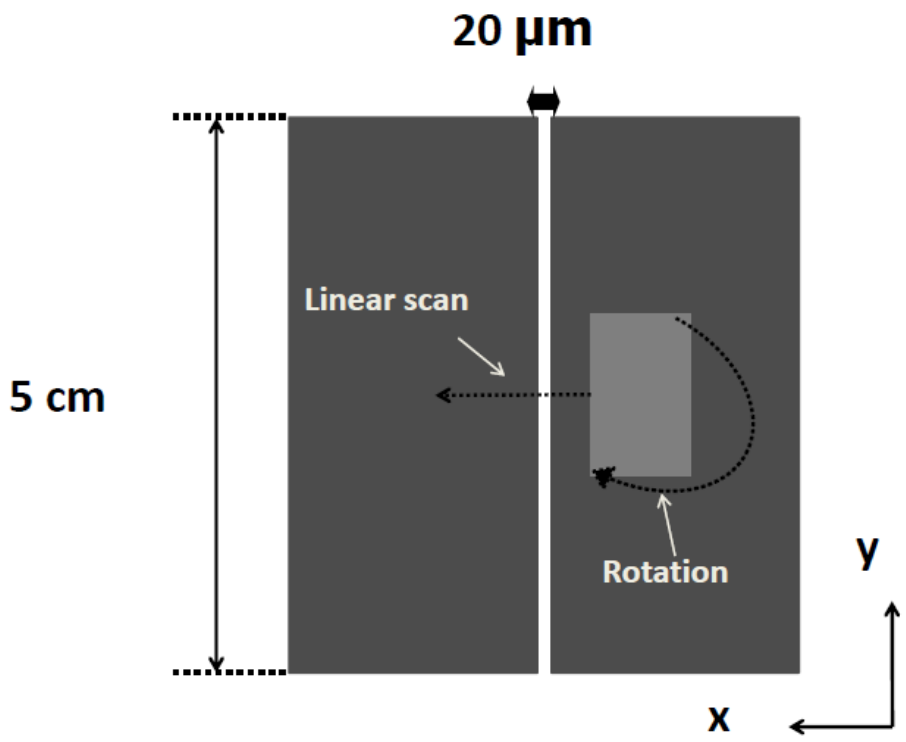

Figure 3.4 Schematics of the sample scanning in front of the imaging probe. The imaging sample is alternately linear scan and rotational scan across the probe. The Rotational scan is in a range of 0° to 175° with a step of 5° and the linear scan is in a range of 0 to 9 mm with a step size of 20 µm.

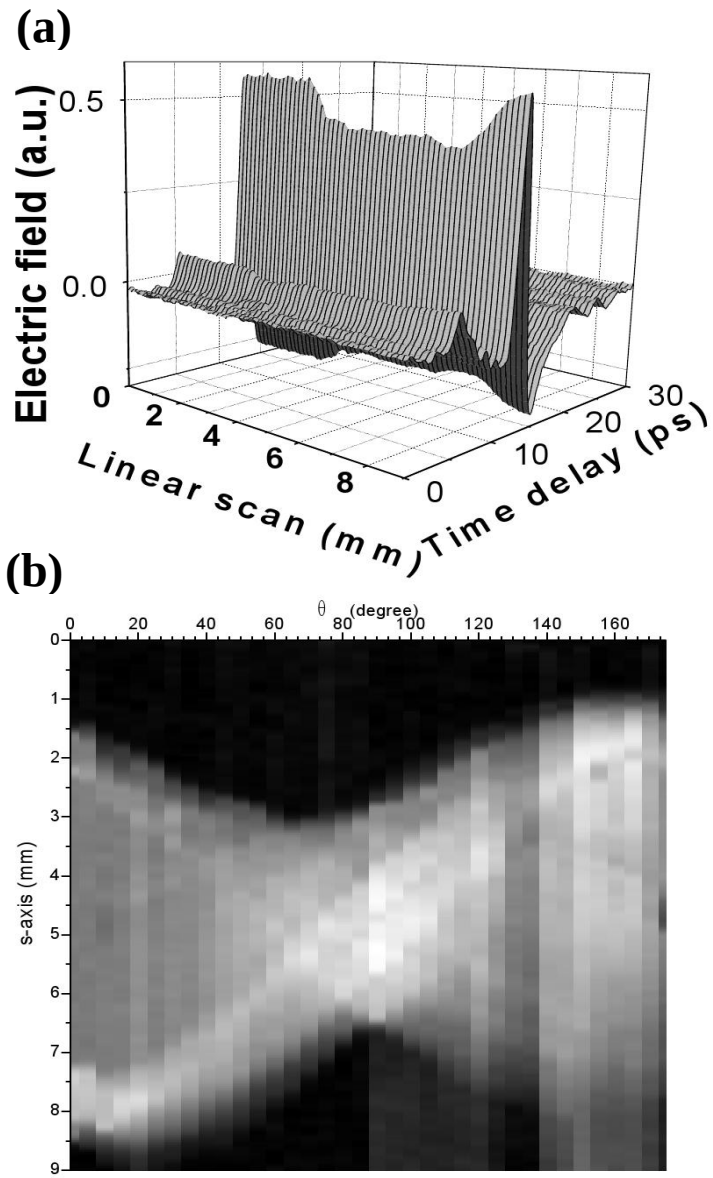

Figure 3.5 (a) Surface plot of one set of time domain signals for a linear scan at angle 0^0. (b) The sinogram of the imaging sample in figure 3.6 (a), the signal amplitude is extracted from spectrum at frequency 0.3 THz.

The sub-wavelength output facet of the tapered PPWG produces high-aspect-ratio illumination with a beam profile that is frequency independent in the x direction (across the plates) and frequency dependent in the y direction (parallel to

the plates) [49, 71, 72]. In our experiment, the input beam has a Gaussian shape with a beam waist of 1.5 cm at the input face of the PPWG, which is considerably larger than the sample size (~4.5 mm). Therefore, it is reasonable to assume the illuminating intensity to be uniform across the illuminated area on the sample in both x and y directions and take a single signal as an integral of the sample information over the output facet area, including topographic and dielectric information.

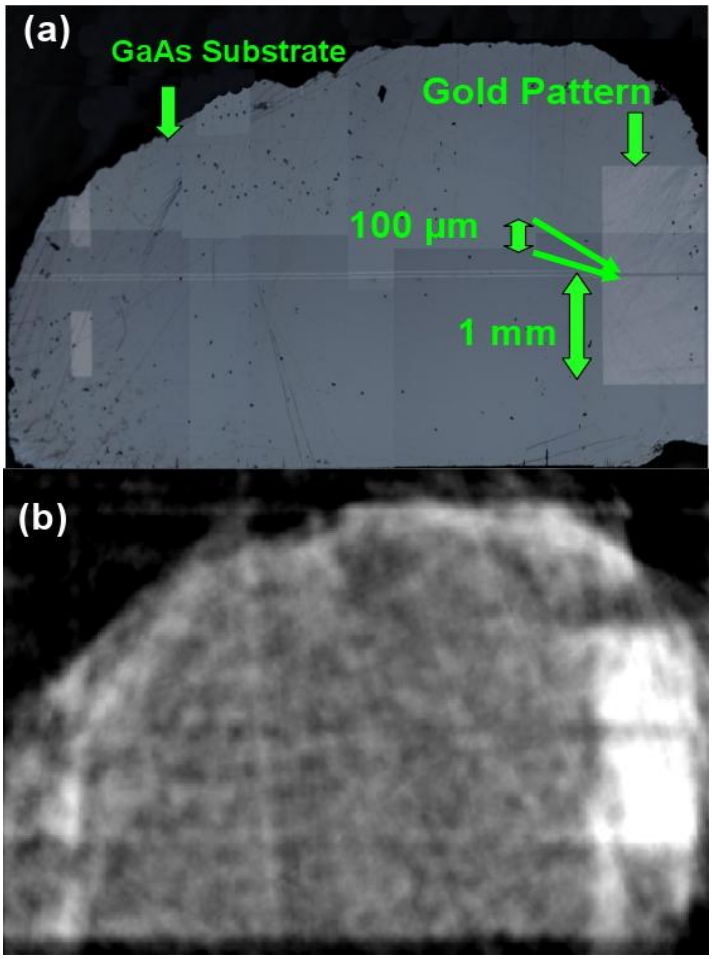

Figure 3.6 (a) Sample image under optical microscope; (b) Reconstructed sample image by the filtered back projection algorithm.

Ideally, the inverse radon transform reconstructs the image from line projections. With our tapered-PPWG probe, the line width is determined by the output face in the minor axis direction, which is 20 μm. So, the resulting image obtained from the FBP algorithm is a convolution of the original image with the system point spread function, which is a two-dimensional Gaussian with the spatial extent of the output facet size [49, 78]. The reconstructed image is shown in figure 3.6 (b), in comparison to an image under optical microscope (fig 3.6 (a)), which has a resolution of a few hundreds nanometers. In the reconstructed image, the GaAs substrate and antenna features as small as 100 μm can be readily identified. A better resolution (~ 20 μm) was not achievable since the sample was not in perfect contact with the output facet. In this work, the imaging processing is performed in MATLAB, and the inverse radon transform is conducted by using the intrinsic function iradon() in MATLAB.

In this chapter, I discussed a tapered PPWG as a probe for broad-band THz near-field imaging. The tapered-PPWG probe reflects part of the incident radiation with information from the near field at the output facet. The reflectance is very sensitive to both the topographic and dielectric information of the sample. This one-dimensionally-tapered-PPWG probe provides a good line illuminator with a high aspect ratio. A single reflection signal is treated as the line integral of the sample information along the probe area. The FBP algorithm is used to reconstruct the image from the spectral amplitude of the average wavelength of 1.5 mm. Features of size ~ 100 μm can be qualitatively identified in the reconstructed image.

Chapter 4

THz Surface Plasmon Polariton: Waveguide Mode of a Finite Width Parallel Waveguide and a Designer THz Resonator Based on Enhanced Reflectivity by Spoof Surface Plasmon

4.1. Surface Plasmon in THz spectrum

4.1.1. Background

Recent interests of surface plasmon polariton (SPP) has been inspired by the observation of extra-high transmission of optical waves through sub-wavelength hole arrays on a thin metal sheet [82]. Similar ultra-high transmissions are also observed in both infrared and THz spectra [37, 83]. The development of surface

plasmon technologies have a lot of practical applications, such terahertz surface plasmon spectroscopy for bio-sensing, planar metal plates surface plasmon waveguide [40, 41, 84].

The metallic response to the electromagnetic waves at terahertz frequencies is relatively less explored experimentally, and it is not exactly predicated by the theory. One example is the wave decay length of surface plasmons into the free space, which was observed shorter in THz range than that predicted by extending the metallic properties from infrared with a traditional Drude model [40, 85]. The surface optical smoothness of the metal sheet is considered as one cause of this difference [40]. In the physical picture, rough surface can be approximately mimiced as a surface with surface gratings or sub-wavelength surface structures, which have been demonstrated to change the propagation properties of the surface waves on the perfect metal surface ([37, 41, 44, 86-88].

4.1.2. Surface Plasmon (Plasmonic) Effect in a Finite Width Parallel-Plate-Waveguide

Parallel-plates waveguide (PPWG) has been the platform for many THz applications, because it has good qualities as a waveguide, such as low-loss no-cut-off and non-dispersion [19]. The early description of the fundamental mode (TEM mode) for a PPWG in THz community was based on the theory developed from microwave frequencies, where the metal is treated as perfect metal boundary [18,

19, 47, 49, 68]. In this description, the PPWG working in the TEM mode has a uniform filed distribution across the space between the metal plates. Recently, the surface plasmon effects on the waveguide mode have been observed at terahertz frequencies for both finite width and infinite width parallel-plate waveguides [71, 72]. When surface plasmon effects play a role in wave propagation in the PPWG, the fundamental mode of the waveguide has more energies confined on the metal surface than in the middle between the two plates [89]. This makes the field distribution across the two metal plates non-uniform, in comparison with that in the traditional TEM mode. When the PPWG has a finite width, the excited edge surface plamons confine more energies at the four corners of the waveguide cross-section[72].

In chapter 4.2, we introduce our work on the characterization of the surface plasmon effect for a finite width parallel-plate waveguide, which works in a fundamental waveguide mode. In our study, we show that the plasmonic effects can be influenced by the geometry of the waveguide, and a sharp waveguide mode transition from the traditional TEM mode to the plasmonic mode is observed at terahertz frequencies.

4.1.3. Spoof Surface Plasmons

As discussed in Chapter 2, surface wave propagations on a planar interface between a dielectric and a metal mostly depend on the electromagnetic responses of

the metal. For an interface between a dielectric (e.g. air) and metal (e.g. Al), there is an asymptotic frequency at which the in-plane wave vector of SPPs reaches maximum. The asymptotic frequency is the up-limit of dispersion curves of surface plasmon polaritons (SPP), which influences the propagation of surface waves. The asymptotic frequency is intrinsically determined by the properties of both the metal and the dielectric, as expressed by equation (4.1),

$$\omega_{asp} = \omega_p / \sqrt{1+\varepsilon_d} \tag{4.1}$$

where ω_{asp} is the asymptotic frequency, ω_p is the bulk plasma frequency, ε_d is the permittivity of the dielectric (In chapter 2).

In terahertz range, most common metals (e.g. Al, Au) in terms of electromagnetic response can be treated approximately as a perfect metal. The energy of the surface waves confine very loosely on the metal surface. However, there are a few ways to change the properties of surface wave on a highly conductive metal surface. One method is to cut a pattern of periodic Bragg gratings on the metal surface. The surface waves on the patterned interface have a strong Bragg reflection at particular frequencies and stop to propagate when interacting with the periodic potential [13, 45, 90]. The Bragg grating changes the propagation properties of the surface waves by forming “artificial band gaps”.

Another completely different method to engineer the dispersion curve of SPP on a metal surface is by using sub-wavelength structures [87, 91, 92]. The metal surface corrugated with sub-wavelength structures supports a well-confined electromagnetic surface wave even for a perfect metal, as if the surface wave propagates on an artificial surface with designed metal properties. This kind of surface plasmon is also called "spoof" surface plasmon. For a metal surface with micro-structures (e.g. periodic rectangular grooves), the collective resonant interaction between propagating electromagnetic wave and reflecting wave from the bottom of the structure significantly slows down the surface wave, making a localized SPP mode.

The dispersion curve of the spoof surface wave is determined by the geometry of the structures. We conducted a simulation using the finite element method for a simple example, that is a perfect metal surface with a set of periodic rectangular grooves [63]. In the simulation, the surface is set as a perfect metal boundary, the periodicity (**d**) of the pattern is 0.024" ($\approx 609\mu m$), the width (**a**) and depth (**h**) of the rectangular groove are 0.006" ($\approx 152\mu m$), and 0.011" ($\approx 279\mu m$), respectively.

Unlike the electromagnetic wave propagation on a bare perfect metal surface, wave propagation on this micro-structured perfect metal surface shows a strong energy confinement on the patterned surface (Fig 4.1). Also the in-plane wave

vectors of the surface wave are different with respect to its frequencies [63] (Fig 4.1(a) and (b)). This is a strong analogy of the surface wave propagates on a metal surface of designed properties (Fig 4.1 (c)). The asymptotic frequency of this metal surface is given by [91],

$$\omega_{sp} = \frac{\pi c}{2h} \tag{4.2}$$

where c is the light speed in vacuum, h is the depth of the rectangular groove.

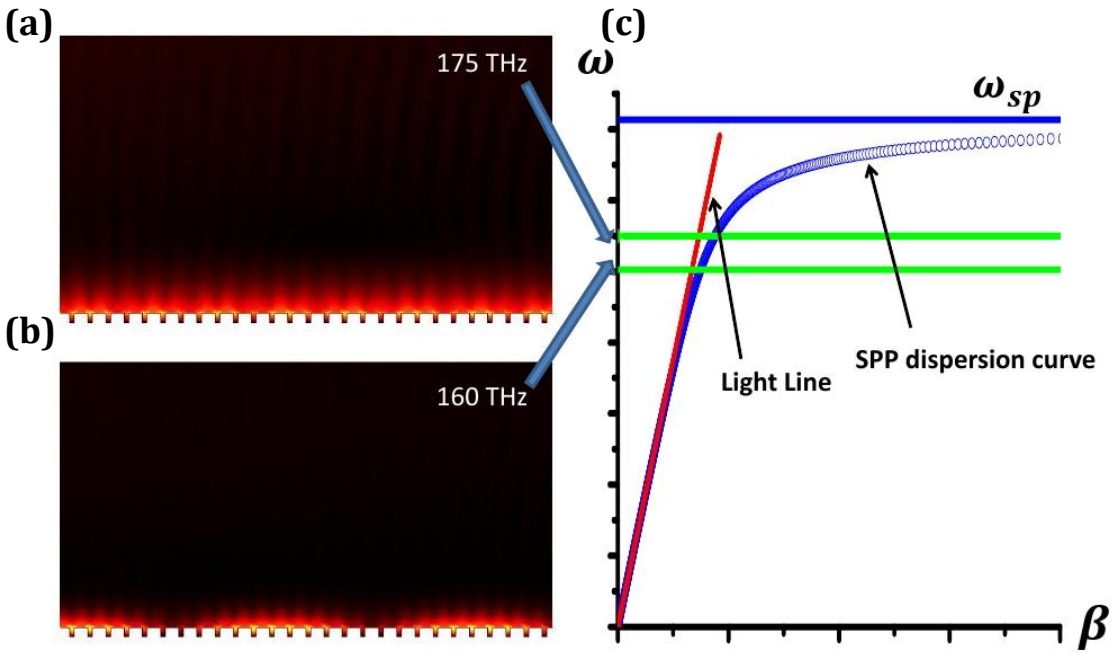

Figure 4.1 (a) The spoof surface plasmon on a corrugated metal surface at 175 GHz. (b) The spoof surface plasmon on the same structured surface at 160 GHz. (c) The dispersion curve of the spoof surface plasmon.

The spoof surface plasmons can be qualitatively interpreted by a standing wave picture at asymptotic frequency [13]. When the surface wave is at the asymptotic frequency, the wavelength is four times of the rectangular groove depth (equation (4.2)). Therefore the groove acts as a resonant cavity along the depth direction. The phase accumulation during a round trip of the groove cavity is 2π, including the phase change of π when wave reflects from the metal surface at the bottom. This cavity resonance dissipates the wave energy and prevent the surface wave from propagating, resulting a band gap at the asymptotic frequency as shown in Fig 4.1 c. When the wave frequency is close to the asymptotic frequency, the surface wave shows a significant deviation from the light line, leading a confined surface wave [13].

The spoof surface plasmon concept has lots of practical applications, such as improving the beam quality and throughput of the THz QCLs [45, 93, 94]. In chapter 4.3, we show another important application of spoof surface plasmon. We revealed that, by patterning the output facet of a parallel plate waveguide (PPWG) with a set of designed grooves, the reflectivity at the output aperture of the waveguide can be enhanced up to 99%. We show detailed characterizations of this enhanced reflectivity by spoof surface plasmon and interpret the observed phenomenon by a theoretical model. A prototype of a novel band-pass THz resonator based on this enhance reflectivity was demonstrated in experiment.

4.2. Waveguide Mode Transition in Finite Width Parallel-Plates Waveguide

Waveguide with a sub-wavelength cross-sectional dimension is an important component for many optical applications, such as that in photonic integrated circuit. In particular, the slot waveguide, which has a geometry consists of two metal plates separated by a small gap, has been studied extensively as a candidate for a sub-wavelength energy confinement and low-propagation-loss waveguide [95, 96]. The fundamental mode for this type of waveguide structure, which is called plasmonic mode, can be excited efficiently and then propagate for a long distance in the waveguide. From another perspective, the slot waveguide is structurally homologous to a finite-width parallel-plate waveguide (PPWG). In the microwave textbook, the fundamental TEM mode of the PPWG has a uniform field distribution along the direction perpendicular to the metal surfaces. And this is generally considered to be a good description of the spatial mode for many experiments in the terahertz (THz) range [19, 47-49, 97]. This mode is, however, quite distinct from the fundamental plasmonic mode of a slot waveguide, even in the case of very wide metal plates. In this section, I show that this distinction is not merely due to the difference in the electromagnetic properties of metals in different frequency regimes but is also intimately related to the geometrical parameters of the PPWG. Using broadband THz time-domain spectroscopy, we observe a rapid transition of

the spatial mode with increasing frequency, from the TEM-like mode of a PPWG to the plasmonic mode of a slot waveguide, in a spectral range where the metal's dielectric properties are essentially frequency-independent. We find that the mode transition is surprisingly abrupt, and can be shifted to higher or lower frequency simply by changing the plate spacing. A geometrically induced mode transition of this type has been discussed over 40 years ago [98-100] but has never been studied experimentally.

In the THz regime, metals are good but not perfect conductors, intermediate between the almost ideal metal (infinite conductivity) at microwave frequencies and the much lower conductivity at optical frequencies, which gives rise to strongly bound surface plasmons. In this intermediate regime, the plasmon decay length δ above a flat metal surface is typically a few wavelengths for real metal structures [40, 41, 85, 88]. As a result, the fundamental mode of a finite-width PPWG depends upon the interplay of three characteristic lengths of comparable magnitude: δ, the free-space wavelength λ, and the distance between the metal plates b. This interplay results in a complex mode behavior, which is readily observable in the THz regime as presented here.

Our experimental approach is based on scattering probe imaging [71, 101], a technique for characterizing the spatial distribution of a THz field with sub-wavelength resolution. The concept is similar to apertureless near-field scanning

optical microscopy (ANSOM) [64]. We mount a subwavelength-sized metal scatterer, typically a short length of thin metal wire, at the end of a dielectric holder. The holder is nearly invisible to THz radiation but the metal object can scatter an incident THz wave toward a receiver. As in ANSOM, the position of the scatterer is modulated using a piezoelectric actuator, so that the signal reaching the detector from the scatterer can be extracted via lock-in detection. Unlike in conventional ANSOM, the detection is phase-sensitive, which has significant advantages [34]. For example, even if the field to be measured is spatially uniform, the differential detection still generates a nonzero signal due to the phase difference induced by modulation of the position of the scatterer relative to the (fixed) THz detector [101].

We use fiber-coupled photoconductive antennas to generate and detect broadband THz pulses. The waveguide consists of two highly polished aluminum plates having a width of 1 cm and a length of 25 cm, assembled with a variable plate separation b. The THz beam incident on the input face of the waveguide is polarized perpendicular to the inner plate surfaces to excite the TEM-like mode, and weakly focused to a spot size of $\sim$ 1 cm. The guided wave propagates along the waveguide until it encounters the scattering probe at a distance of 22.5 cm downstream of the input facet. The scattering probe is positioned between the two metal plates, equidistant from both. It oscillates at a frequency of 180 Hz with an amplitude of $\sim$1 μm, and can be translated into and out of the PPWG, along a line perpendicular to the waveguide axis.

Fig 4.2 shows typical waveforms detected at three different locations. The upper-right inset illustrates a cross-section of the PPWG with dots indicating the measurement locations. The lower-right inset shows the corresponding Fourier-transformed spectra, which can be used to characterize the frequency-dependent-

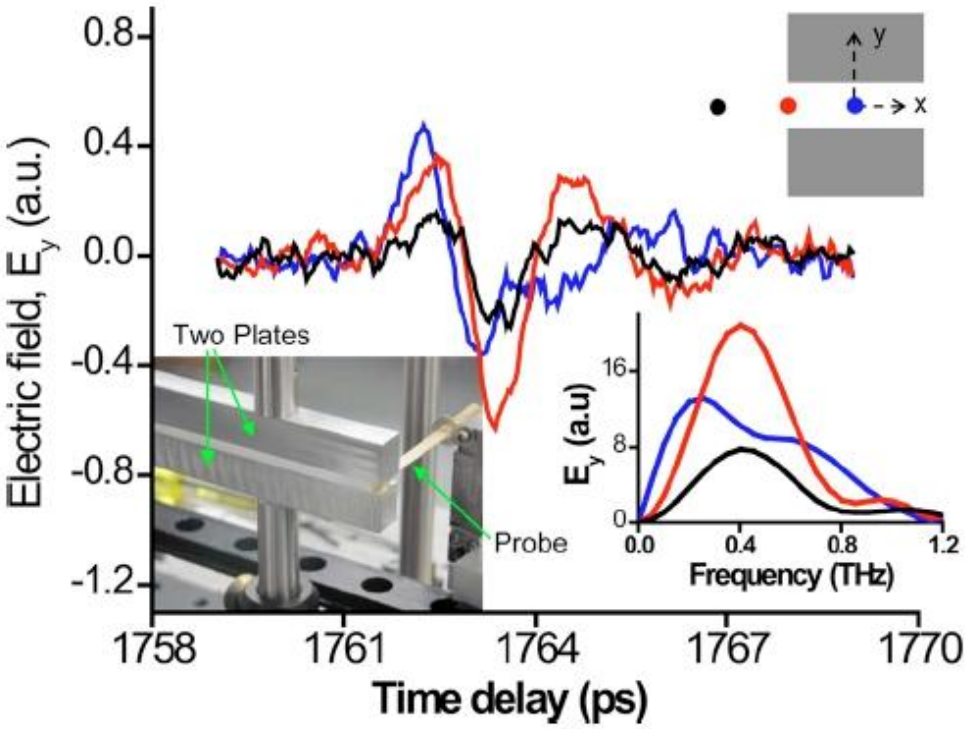

Figure 4.2. Signals measured inside (blue), at the edge (red), and outside (black) of the waveguide. These locations are illustrated by the cross-sectional view in the upper-right inset. The lower-right inset shows the corresponding spectra, which all have spectral bandwidths similar to that of the input THz pulse. These indicate that the scattering probe technique does not introduce any significant spectral distortion or bandwidth limitation on the measured signals. The left inset shows a photograph of the PPWG with the scattering probe inserted between the plates. The plate-width along the x direction is 10 mm.

-spatial field distribution. Since the PPWG is symmetric with respect to the axial plane perpendicular to the plate surfaces, we only need to scan the probe through one half of a transverse plane to map the full distribution. We plot the spectra for each measurement position, and normalize these plots to unity for each frequency, to emphasize the evolution of the spatial distribution of the field with frequency. This result is presented along with its mirror image for clarity in Fig. 4.3 (a), which shows the result for three different plate separations.

We observe a dramatic evolution in the field distribution with increasing frequency, which depends strongly on the plate separation. At low frequencies, the energy is concentrated in the center of the waveguide (x=0), as one would expect for the TEM mode [102]. However, at higher frequencies, there is a sharp transition to a different mode, where the energy is concentrated near the waveguide's edges at x = ± 5 mm. This high-frequency field distribution is strongly reminiscent of the mode of a slot waveguide exhibiting edge plasmons, which has been predicted for optical frequencies [95] and observed in the infrared [103] and THz [71, 72], using near-field measurements. All three panels in Fig. 4.3 (a) show qualitatively similar behavior, except that the frequency at which the transition occurs changes with b. This indicates that the transition from a TEM-like mode to a plasmon-like mode is determined by geometrical parameters, e.g., the dimensionless ratio b/δ or b/λ. Evidently, at a particular wavelength one can observe either mode (or any intermediate hybrid [98-100] simply by varying b. Figure 4.3 (b) shows numerical

two dimensional simulations of the experimental configuration, based on the finite element method [63]. These simulations do not account for diffractive losses at the waveguide edges, an effect which is larger for lower frequencies. Thus, the low frequency centralized mode does not weaken at the edges of the PPWG, as it does in the experiments. Nevertheless, the mode transition is accurately reproduced, as well as its sensitivity to b.

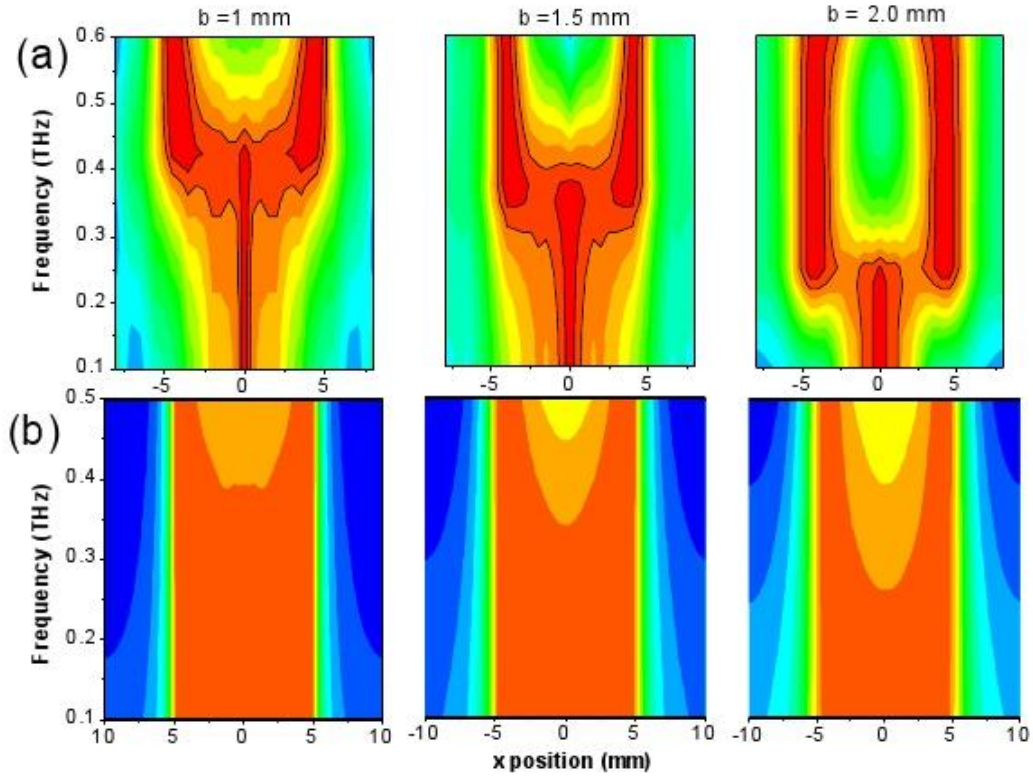

Figure 4.3 Contour plots of the normalized cross-sectional electric field distribution based on (a) experimental data and (b) numerical simulations using the finite element method. The horizontal axis gives the location of the measurement and the vertical axis gives the frequency. The waveguide

extends from x=−5 to 5 mm. Each row of these figures has been normalized to unity, in order to remove the spectral dependence of the input pulse and emphasize the frequency-dependent mode transition. Results for three different values of the plate separation b are shown.

We can further analyze the results of Fig. 4.3 (a) to understand the mechanism responsible for the spatial mode transition. From these results, we extract a characteristic frequency at which the transition from the TEM-like mode to the plasmon-like mode occurs. We plot two vertical slices, at the waveguide center (x=0) and edge (x=5 mm), and define the transition frequency as the cross-over point of these two spectral curves. A typical pair of such curves, for b =1.5 mm, is shown in the inset of Fig. 4.4, which plots the transition frequencies determined in this manner for various values of b (circles).

We can interpret the approximate inverse relationship between the transition frequency and b via an intuitive argument based on surface waves. When b is much smaller than the decay length δ, there is strong coupling between the surface waves propagating on the two plates. Thus, the field amplitude is nearly constant along a line from one plate to the other, and the mode is similar to the conventional uniform TEM mode [89, 95]. However, when b is comparable to or larger than δ, then the mode begins to more closely resemble two-independent surface waves, one on each metal surface, analogous to the hybrid mode described by Barlow [98-100]. For finite-width PPWGs, this field distribution also shows

strong enhancements at the edges due to the excitation of edge modes [71, 95]. Therefore, the degree of interaction between the two surface waves strongly influences the transition frequency.

We can develop a simple theoretical model to compute this transition frequency and compare to our experimental results. We use the analytical expressions for the TM polarized waves between two metal plates of infinite width [89], and model the metal using Drude theory [104]. From these expressions, we can numerically compute the value of the electric field E(y), along the y axis (perpendicular to the plate surfaces). For any chosen value of λ and b, we can then compute the fractional difference Δ between the electric fields at the plate surface and half-way between the surfaces as $\Delta = [E(0) - E(b/2)] / E(0)$. For an ideal TEM mode, $\Delta = 0$; for two noninteracting surface waves, $\Delta = 1$. Selecting an arbitrary criterion of $\Delta = 0.05$ as the signature of departure from the low-frequency behavior, we can calculate the transition frequency as a function of b. The prediction of this model, plotted as a solid line in Fig. 4.4, agrees reasonably well with the transition frequencies extracted from the experimental data.

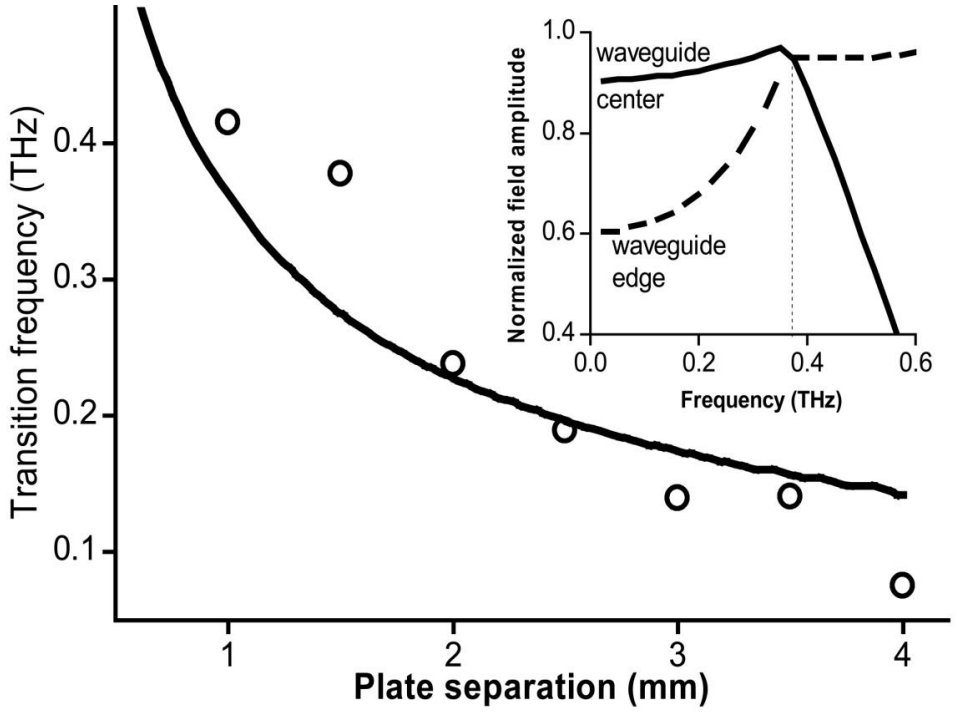

Figure 4.4. The transition frequency as a function of the plate separation b. The black circles are the experimental results and the solid line is the calculated curve from the theoretical model described in the text. The inset shows two vertical cuts extracted from the data of Fig. 4.3. (a), for b=1.5 mm. The crossover point of these two curves defines the transition frequency.

In summary, we have conducted frequency-resolved measurements of the spatial mode pattern of a propagating wave inside a finite-width PPWG. We observe a surprisingly abrupt transition in the guided mode, from a TEM-like mode (with energy concentrated in the center of the waveguide) to a plasmon-like mode (with energy concentrated at the edges). The frequency of the mode transition depends on the geometry of the PPWG, i.e., the plate separation. This is likely to be a general result for many types of plasmonic waveguides, and indicates that the behavior of

guided plasmon waves can be influenced as much by geometrical effects as by the dielectric properties of the metal components.

4.3. Enhanced Reflection by Spoof Surface Plasmon Polariton

As we discussed in the introduction, bound surface waves are not supported on the surface of a perfect metal with infinite conductivity. However, by adding structure to an otherwise smooth metal surface, it becomes possible for the surface to support a tightly bound surface wave, known as a spoof surface plasmon (SSP) [44, 87, 91, 105]. A promising aspect of SSPs is that their properties can be controlled in a range of frequencies by changing the geometry of the patterned structures[38, 106]. Many of these previous studies involving THz SSPs have been focused on enhancing transmission through a subwavelength structure; the idea of using SSPs for enhancing reflection has not been explored.

In the previous project in this thesis, we have characterized the impedance mismatch at the output facet of parallel-plate waveguides (PPWG) and explored their application as THz near-field imaging probes (Chapter 3) [75, 107]. We choose a PPWG as a design platform because of its popularity as a prototype guided wave structure in the THz region. With a TEM mode having no cut-off, negligible group velocity dispersion, and low ohmic losses, the PPWG has proven to be a useful platform for many applications involving THz pulses[49, 68, 69, 108, 109].

Basically, when an electromagnetic wave propagating in the TEM mode in a parallel-plate waveguide encounters a sharp termination of the waveguide, there is a discontinuity of the impedance from the characteristic impedance of the PPWG to the impedance of free space (~377 Ω). Thus there is a reflection at the output aperture resulting from the impedance mismatch, which increases as the plate spacing decreases[75, 107].

Structuring the output facet can allow us to change characteristic impedance of the spoof surface plasmons and therefore control aspects of this impedance matching. Many of these previous studies involving THz SSPs have been focused on enhancing transmission through a subwavelength structure; the idea of using SSPs for enhancing reflection has not been explored. In this section, we explore the possibility of minimizing the power flow from the waveguide by using spoof surface plasmons, so as to engineer a high reflector at the waveguide facet.

4.3.1. Enhanced reflection using spoof surface plasmons

Our device is based on an aluminum PPWG. To support SSPs on the output surface, a periodic pattern of straight grooves are cut into the output facet of both the upper and lower waveguide plates, parallel to the output aperture of the waveguide. The groove patterns on the two waveguide plates are identical to each other. Figure 4.5 (a) illustrates a cross-section of a pattern of five periodic grooves on the output facet, adjacent to the waveguide's exit aperture. The cross-section of a

single groove is rectangular, with a fixed width (*a*) of 152 μm. The plate spacing (*b*), groove depth (*h*), periodicity (*d*), and the distance from the first groove to the waveguide aperture edge (*L*) are varied to tune the frequency and strength of the surface plasmon coupling [45, 87, 92, 93, 110]. The incident angle θ of the incoming beam is varied in the experiment to characterize the reflectivity of the patterned facet as a function of angle (Fig. 4.5 (b)).

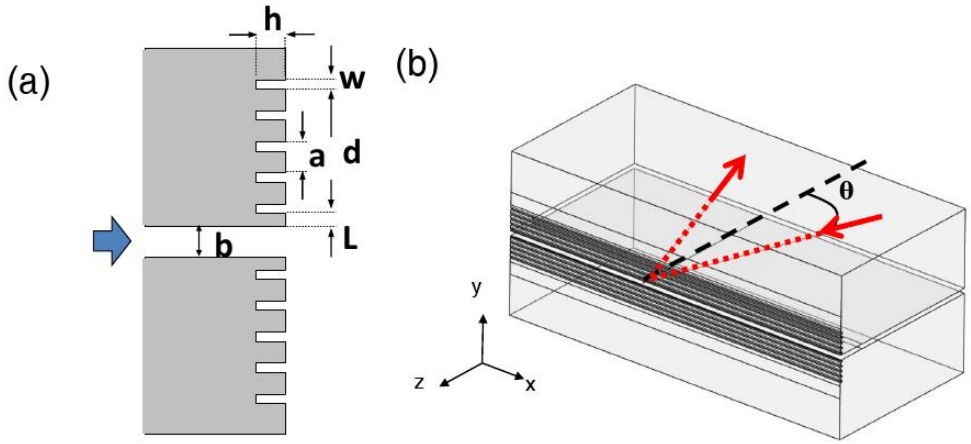

Figure 4.5 Schematic of waveguide with groove pattern

To fine tune the geometrical parameters of the groove pattern for the highest reflectivity, we conducted numerical simulations using the finite element method (FEM) [63]. Figure 4.6 (a) shows an example of the optimized reflectivity. The plot illustrates the simulated reflection coefficients as a function of frequency with the

parameter settings as indicated in the inset. At the selected frequency (174 GHz), the reflection coefficient at the output facet reaches a peak of more than 99% (peak reflectivity). The red curve shows a simulation using the same PPWG without groove patterns on the output surface, in comparison to the case with five grooves on each plate. Clearly, the reflection is greatly enhanced relative to that of a waveguide without any groove pattern (which is ~20% for this plate separation). Figure 4.6(b) shows a cross-sectional plot of the electric field distribution in the neighborhood of the output aperture at the design frequency (174 GHz). Most of the energy concentrates in the near field in the vicinity of the grooves and the output face of the waveguide, showing no energy coupling out into the far field. The number of grooves on each plate of the PPWG also has an influence on the reflectivity, as shown in Fig. 4.6 (c). As the number of grooves increases, the peak reflectivity increases to nearly 100%, saturating when the number is larger than about four. Evidently, almost all of the contribution to the enhanced reflectivity is from the first five grooves, so for our experimental studies discussed below we choose to cut five grooves on each plate of the PPWG.

Further simulations permit us to investigate the dependence of this enhanced reflectivity (R) on various aspects of the groove pattern geometry. These simulations are an important aspect of the fabrication and optimization process. Figure 4.7 illustrates the enhanced reflectivity as a function of several relevant geometrical parameters (*h*, *d*, *L*, and *b* as defined in Fig. 4.5), extracted from

numerical simulations. In Fig. 4.7, each panel illustrates the results of a series of simulations in which we sweep the value of a single parameter in a range around the optimized value (indicated by the dashed line in each panel), with the other geometrical parameters fixed at the values indicated in Fig. 4.6(a). Two key factors are extracted from the simulations and plotted in this figure: one is the highest value of the reflectivity R exhibited at any frequency within the simulation range, and the other is the frequency at which R reaches this maximum value (labeled as the peak frequency).

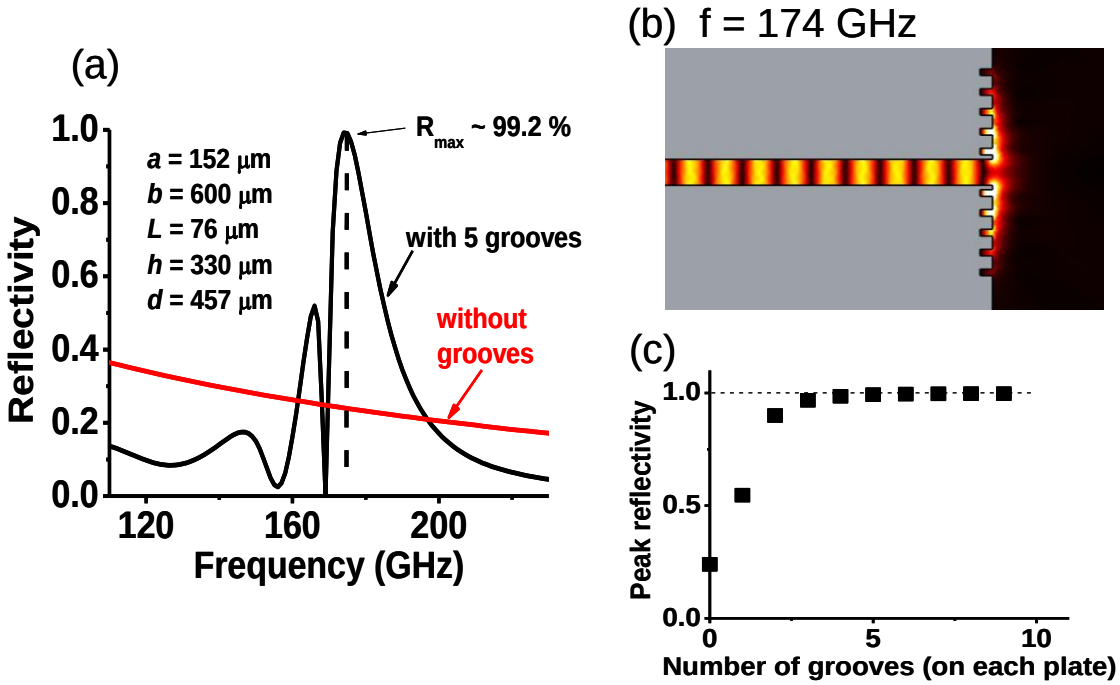

Figure 4.6 (a) Simulated reflectivity as a function of frequency for the PPWG with the groove pattern defined by the parameters indicated in the inset. The red curve shows the reflectivity of the same waveguide except with no

grooves. (b) A false-color plot of the electric field amplitude adjacent to the output aperture of the PPWG at the selected resonant frequency. (c) Peak reflectivity as a function of the number of grooves on each plate.

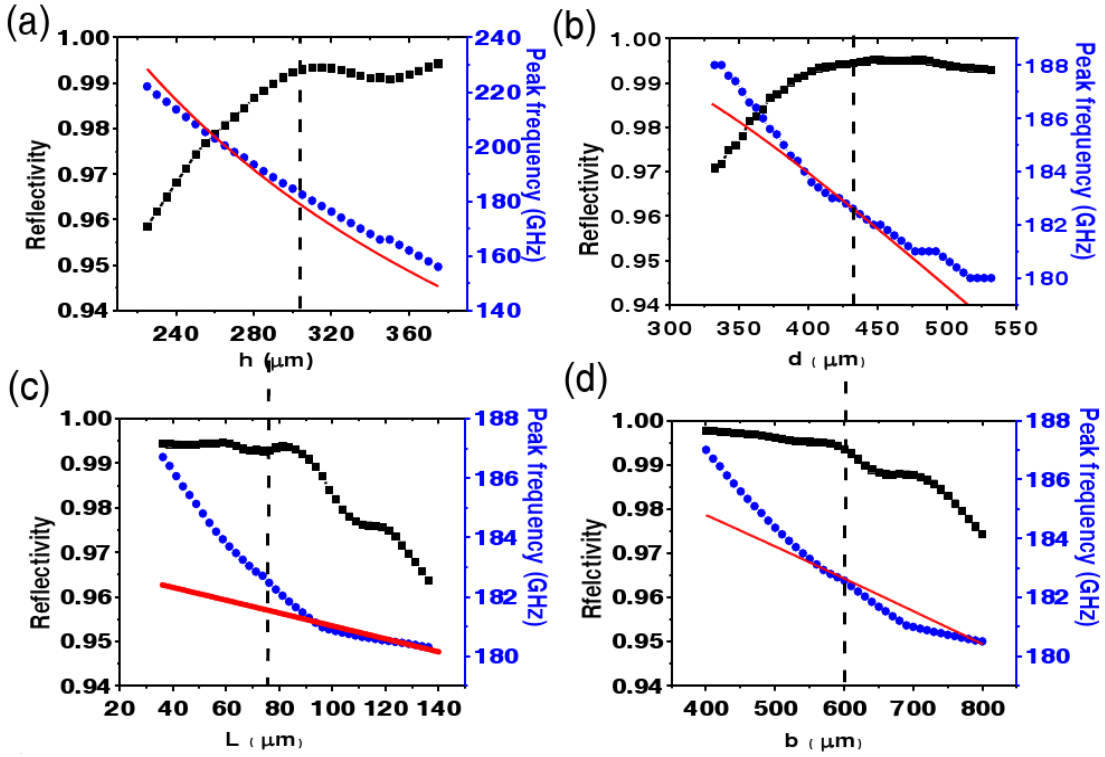

Figure 4.7 The reflectivity (black squares) and peak frequency (blue circles) as a function of (a) groove depth, (b) groove periodicity, (c) the distance between the first groove and the edge of output aperture, and (d) the plate spacing. In these simulations, one parameter is varied while all of the other parameters are fixed at the values shown in Fig. 2(a).

As shown in Fig. 4.7(a), both the peak frequency and reflectivity are very sensitive to the groove depth (h). This can be understood by using the asymptotic

frequency ($\omega = \pi c/2h$) of the SSPs, which is designed to enhance reflectivity at the open end of the waveguide. When the groove depth becomes shallower, the asymptotic frequency blue shifts, and thus the SSPs with the same surface confinement have a higher frequency. The periodicity (*d*) of the pattern also influences the behavior of the supported SSPs, but with less sensitivity than *h* (as in Fig. 4.7(b)). The SSPs have an effective wave vector k_x parallel to the metal surface. For the 1-D groove pattern, k_x can be approximately expressed by the dispersion relation [91, 110],

$$k_x = k_0 \sqrt{1 + \frac{a^2}{d^2} \tan^2 k_0 h} \qquad (4.3)$$

where k_0 is the wave vector in vacuum, and *a*, *h* and *d* are the groove width, groove depth, and the periodicity of the groove pattern, respectively. The periodic grooves also act like a grating with a band edge determined by $k_{x1} = \pi/d$. This grating resonance also contributes to the resonant coupling between the waveguide mode and the SSP mode. The periodicity *d* decreases as the inverse of the band edge k_{x1}, corresponding to a high frequency on the dispersion curve (Fig. 4.7(b)). The distance between the first groove and the edge of the waveguide aperture (*L*) also influences the interaction between the SSP mode and waveguide mode. The longer the distance *L*, the less the coupling between waves of the two modes, and therefore the less reflectivity. We note that this behavior is not linear, but rather exhibits a

threshold behavior, with a rapid decrease in reflectivity for L larger than about 90 μm (Fig. 4.7(c)). The plate spacing (b) influences the effective impedance of the TEM mode in the PPWG [75, 107], as well as the diffraction of the waves at the output aperture. Because the enhanced reflection results from the resonant coupling of two modes which have wave vectors orthogonal to each other [111], the coupling efficiency depends on the mode matching at the output of the waveguide. The smaller the plate spacing, the more the waves at the output aperture are strongly diffracted, and thus the better coupling to the modes with orthogonal wave vectors, leading to a larger enhanced reflectivity (Fig. 4.7(d)). It is clear from these simulations that, within the tolerance of mechanical machining (~ ±25 μm), it is possible to design and fabricate waveguides with groove patterns optimized for high reflectivity (>99%) at a selected frequency of interest. Small errors in the groove geometrical parameters can be offset by slightly adjusting the plate spacing b so as to obtain the desired resonant frequency for maximum reflectivity.

We can gain a qualitative understanding of the dependence of the peak frequency on the geometrical parameters of the groove structure using a simple RLC circuit model (Fig. 4.8). Because the plate spacing b of the PPWG and the sizes of the grooves are subwavelength in scale, the whole structure can be represented as a short dipole antenna as illustrated in Fig. 4.8(a). In this picture, the PPWG acts as the feeding circuit and the corrugated output facet acts as the antenna pad. The equivalent circuit model is shown in Fig. 4.8(b). To analyze this model, we write the

effective length of one arm of the dipole antenna as $x = b/2 + L + \eta d$, which is equivalent to the physical size of the corresponding waveguide structure. Here, η represents the number of grooves in which the SSP field amplitude is significant. As shown in Figs. 4.6(b) and 4.6(c), when the waveguide mode and the SSP mode are resonant, most of the energy concentrates on the first three grooves, so we estimate $\eta \sim 3$. In this case, the capacitance of the structure can be approximated as that of a linear dipole antenna [112, 113]:

$$C \approx \frac{\pi \varepsilon_0 \cdot x}{\log(x/h)} \tag{4.4}$$

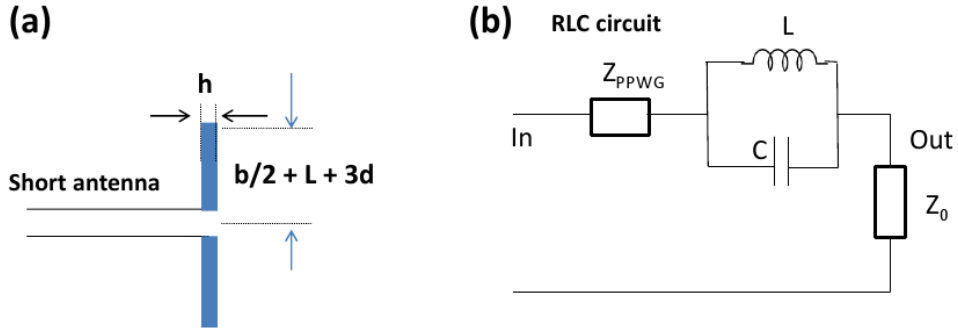

Figure 4.8 (a) A schematic of the antenna model discussed in the text. (b) The equivalent RLC circuit for the antenna model.

The inductance of the short antenna can be calculated as the ratio of the magnetic flux φ to the current I. According to the numerical simulation, when the waveguide and SSP are at resonance, most of the magnetic field lines are concentrated inside the grooves. The magnetic flux can thus be estimated by using the average magnetic field times the area of the grooves ($\eta \cdot ah$). Since the antenna current is fed by the PPWG, it is not influenced by the groove structure and is therefore a constant value. Thus, the inductance is approximately proportional to the groove area. For the circuit of Fig. 4.8 (b), the resonant frequency is calculated as $\omega = 1/\sqrt{LC}$. From this, we find an approximate proportionality which predicts the scaling of the resonant frequency with geometrical parameters:

$$\omega \propto \sqrt{\frac{\log(x/h)}{\eta ah \cdot \pi\varepsilon_0 x}} \tag{4.5}$$

This expression can be used to understand the functional dependence of the resonant (peak) frequency on the geometrical parameters h, b, L, and d. As illustrated by the red curves in figure 4.7, the predictions of this simple analytical model, with a suitably chosen proportionality constant, show reasonable consistency with the FEM numerical simulations.

The schematic of the experimental setup for the normal-incidence reflectivity measurement is shown in Fig. 4.9. A THz-TDS system using a fiber-coupled transmitter and receiver are used, with a bandwidth ranging from 0.01 THz to 2

THz. The THz wave is polarized normal to the aluminum plates in order to excite the TEM mode at the input of the waveguide. A Teflon cylindrical lens is held adjacent to the input aperture of the PPWG to improve the coupling efficiency into and out of the PPWG [19]. A 2 cm thick high-resistivity silicon beam splitter is used to sample part of the reflected beam into the THz receiver. We use a thick silicon beam splitter so that its etalon reflections can be temporally separated from the signal of interest. The reflected signal from the output facet of the PPWG is measured by the receiver with a long time window to achieve high spectral resolution. Since the incident and reflected beams are overlapped and are normal to the PPWG output face, the measured signal is the normal reflection as indicated in Fig. 4.9.

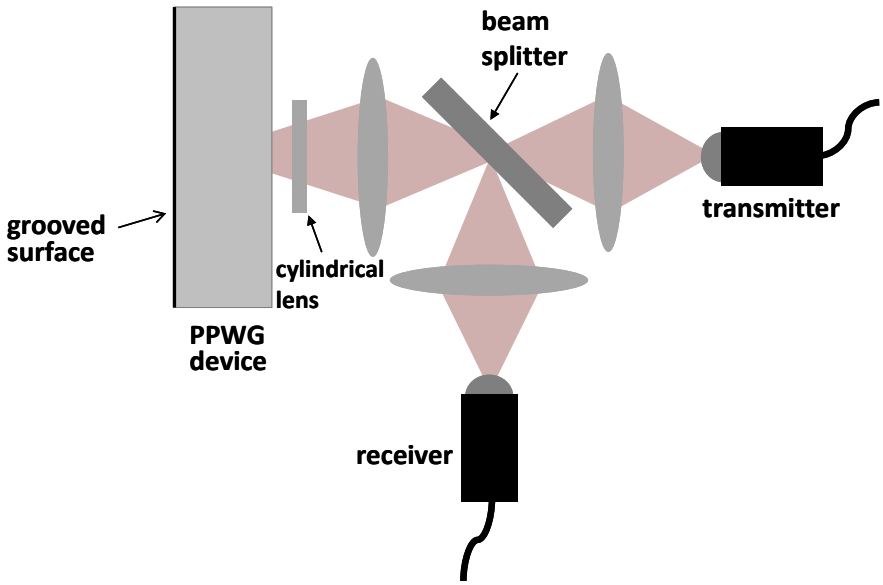

Figure 4.9 The experimental setup for normal-incidence reflection measurements.

A series of waveguides with each plate having a 5-rectangular-groove pattern of different parameters were fabricated and tested in our setup. Figure 4.10 shows typical examples of transmission and reflection for two sets of waveguides. One set has a plate spacing of b = 600 μm (Fig. 4.10(a) and 4.10(c)), while the other has a separation of 200 μm (Fig. 4.10(b) and 4.10(d)). The transmitted signals are collected by putting the receiver on the optical axis 2cm away from the output of the waveguide. These transmission spectra are normalized to the transmission spectra through a waveguide of identical dimensions without grooves. For reflection, a reference signal was measured by pressing an aluminum mirror directly against the output facet, so that the reference signal represents a nearly perfect reflection at the output facet.

For the waveguide of plate spacing of 600 μm, two different 5-groove patterns are tuned (by choosing L, h, and d) for two distinctive frequencies, 83 GHz and 197 GHz. Figures 4.10(a) and 4.10(c) show that the transmission is strongly diminished and the reflection enhanced (>99%) at the design frequencies for both cases. These results are in reasonable agreement with numerical simulations (solid curves). For waveguides of plate spacing of 200 μm, the groove patterns are also optimized for two different frequencies, 179 GHz and 234 GHz. Similar strong modifications of the spectrum are shown in Figs, 4.10 (b) and 4.10 (d), which also shows a reflection coefficient approaching 100%. These results demonstrate that the peak frequency can be tuned by modifying the geometrical parameters of the

metal surface structuring, while maintaining the near-perfect reflection at the design frequency.

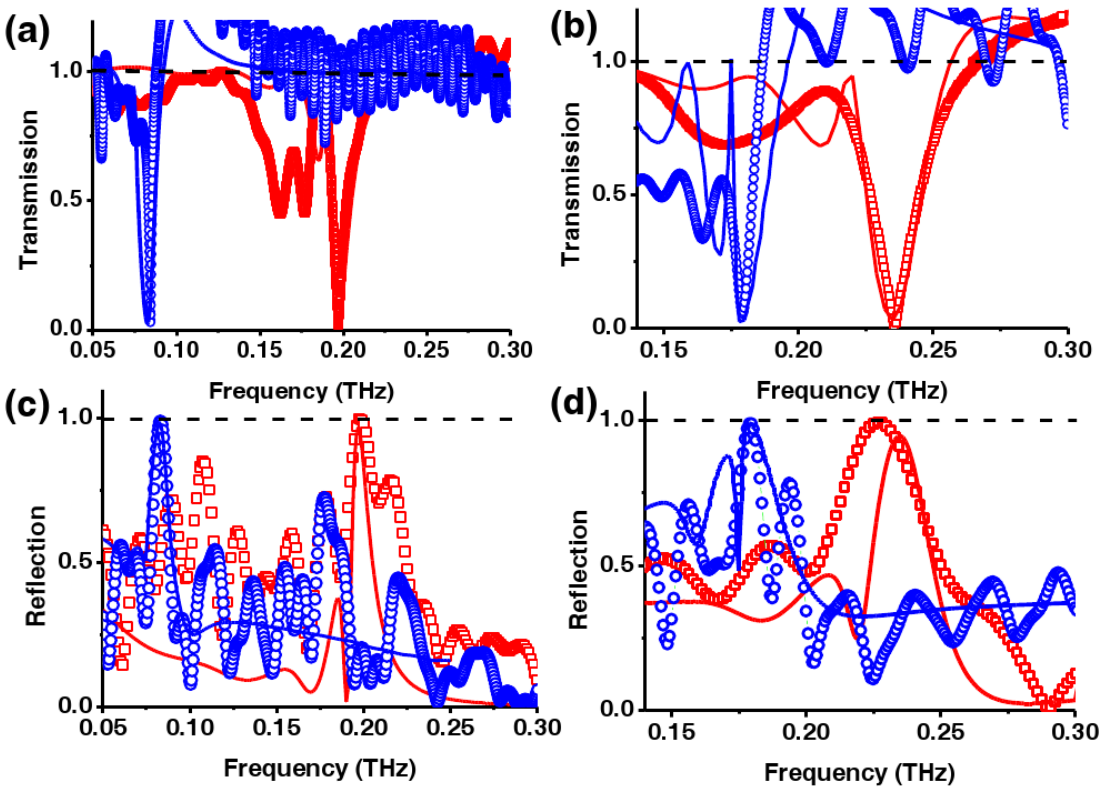

Figure 4.10 (a) Normalized transmission spectra for the devices of plate spacing 600 μm with designed resonant frequencies at 83 GHz and 197 GHz. (b) Normalized transmission spectra for devices of plate spacing 200 μm with designed resonant frequencies at 179 GHz and 234 GHz. (c) Normalized reflection spectra for the same devices as (a). (d) Normalized reflection spectra for the same devices as (b). In all four panels, the squares and circles indicate the experimental results, while the solid lines show the results of the corresponding numerical simulations.

We note that a PPWG which has a plate spacing of 200 μm exhibits a reflection at the output aperture of ~60% even with no groove pattern, because of the impedance-matching consideration discussed above [75, 107]. Thus to differentiate the reflectivity enhancement by SSPs, it is clearer to use PPWGs of spacing 600 μm, for which the reflection coefficient is less than 20% at the frequencies of interest when the output facet is not patterned with grooves. In this case of larger plate spacing, the reflectivity change (grooves vs. no grooves) is more than a factor of five.

4.3.2. Angle Effect and Phase Shift

An essential investigation on this SPP promoted reflectivity is to probe the resonant coupling between TEM mode in the PPWG and the surface plasma mode on the patterned surface by varying the incident angle (θ) (Figure 4.5). For the angle-dependent measurements, we fabricate a new series of waveguides with an angled facet on the input side in a way that the input and reflected waves both travel through the waveguide facet that is normal to the propagating direction (as shown in the inset Fig. 4.11). For all angles the waveguides have an identical groove pattern tuned for highest reflection at a frequency of 191 GHz for normal incidence. For each incident angle, the THz receiver covered by an aperture of 1mm is put 2 cm away from the waveguide facet where the reflected wave comes out.

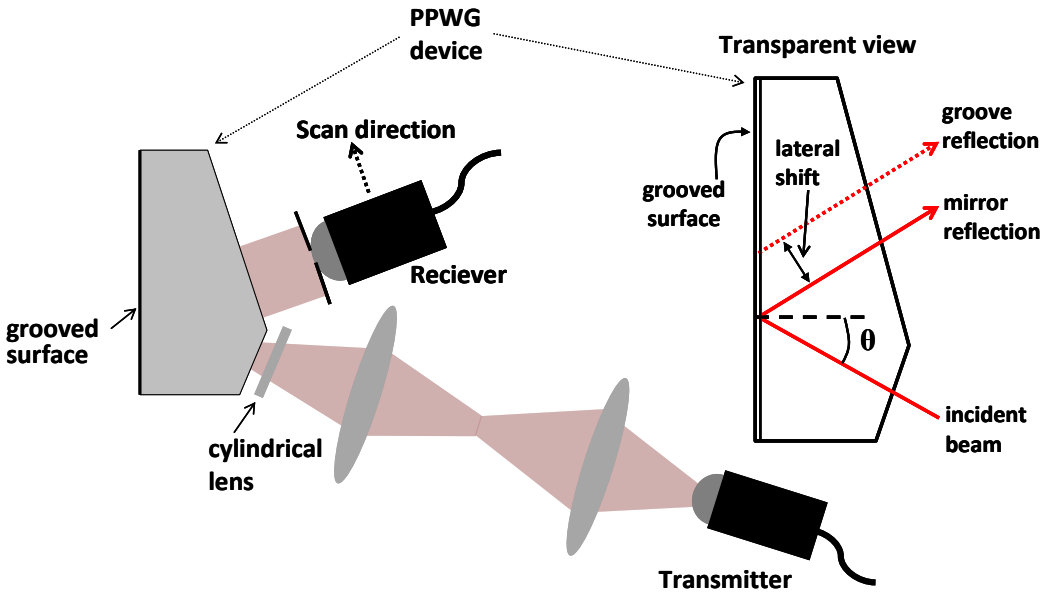

Figure 4.11 Experimental setup for the measurement of reflection at an oblique angle of incidence, θ > 0. The right inset shows a ray tracing schematic of the device designed for the measurement of the lateral spatial shift of the reflected beam as a function of angle of incidence.

As indicated in figure 4.12, the peak frequency at which the reflection reaches the maximum makes a blue shift as the incident angle increases, which is consistent with the 3D simulation using finite element method (red curve). The peak frequency shift follows a functional form of dependence on incidence angle as represented in the equation $f * \cos\theta = f_0$, where f is the peak frequency, θ is incident angle and f_0 is the designed frequency (191 GHz) for normal incidence that is determined by groove geometry. A plot of the equation is shown in the inset of

figure 4.12 along with the experimental and simulation results, which show an excellent agreement.

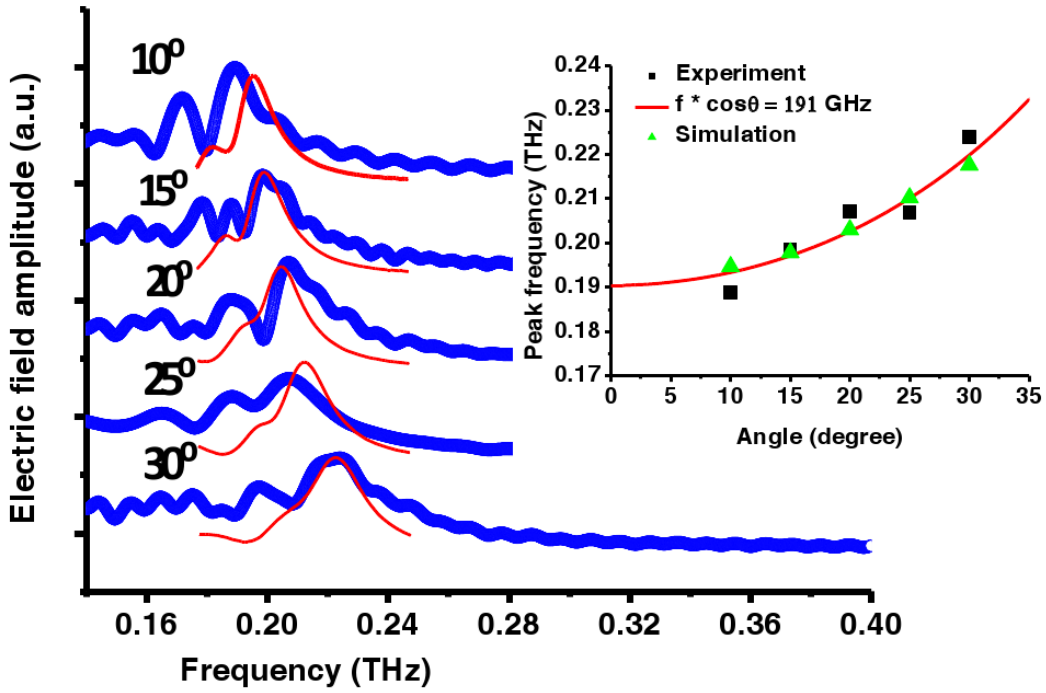

Figure 4.12 Dependence of the spoof surface plasmon enhanced reflectivity on the incident angle. (Dotted blue lines show the experimental data; Solid red lines show the simulation data).

We also note that, as the incident angle increases, we observe a decrease in the peak reflectivity, from almost 99% at 10° to only 84% at 30°. This can be understood as follows: when the incident wave has a k-vector component parallel to the groove direction (the x axis in Fig. 4.5(b)), part of the energy can couple into a groove waveguide mode propagating along the groove axes. This mode, which is an

analog of the channel plasmon [114, 115], can lead to energy loss for the reflected wave. The amount of the energy loss in this way depends on the coupling efficiency which is an increasing function of the incident angle. Therefore the incident angle should be kept low in the application design in order to obtain high reflectivity.

It is clear from these data that there must be an interaction between the guided mode inside the waveguide and the spoof surface plasmon mode on the output facet. We employ a model in which this interaction is described by the difference between two orthogonal wave vector components. We represent this wave vector difference by κ, defined as $\kappa = k_{W,z} - k_{SSP,y}$. Here $k_{W,z}$ is the z component of k_W (the wave vector of the TEM mode inside the waveguide), and is given by $k_{W,z} = (\omega/c)\cos\theta$. $k_{SSP,y}$ is the y component of the wave vector of the SSP at the design frequency for maximum reflectivity at $\theta = 0$. Since the design frequencies for our devices correspond to wavelengths that are large compared to the periodicity of the structure, $k_{SSP,y}$ is approximately given by ω_0/c, where ω_0 is the design frequency [92] . Thus, we find:

$$k = (\frac{\omega}{c})\cos\theta - \frac{\omega_0}{c} \tag{4.6}$$

We then assume that the amplitude reflection coefficient $r(\omega,\theta)$ at the waveguide output facet can be written in the form:

$$r(\omega,\theta) = A(k^2)e^{i\varphi(k)} \tag{4.7}$$

where A(x) is a lineshape function and Φ(x) is a phase function, both of which are unknown functions depending on κ as shown. The angle dependence of the frequency of the reflectivity maximum can then be derived by setting the partial derivative $\partial A/\partial\omega$ equal to zero, which immediately yields:

$$f_{peak} = f_0 / \cos\theta \tag{4.8}$$

This equation is equivalent to the equation we used to plot the inset in figure 4.12. The agreement of the simulation, the experimental data and the plot shows a good proof of this model.

The coupling between two orthogonal wave vector components (eq. 4.6) can have important implications that are revealed by studying the angle dependence of the reflection. For example, this coupling introduces a lateral shift in the position of the reflected beam, comparing to the reflected beam by a mirror placed at the output facet of the waveguide. This lateral displacement Δ is reminiscent of the Goos-Hänchen effect, especially in cases where the reflecting medium is metallic [116-118]. Both effects can be explained as being the result from the propagation of an evanescent wave parallel to the interface. However in the traditional Goos-

Hänchen effect the wave vector of the evanescent wave lies in the plane of incidence, whereas in our case the reflectivity is mediated by the wave vector component perpendicular to the plane of incidence.

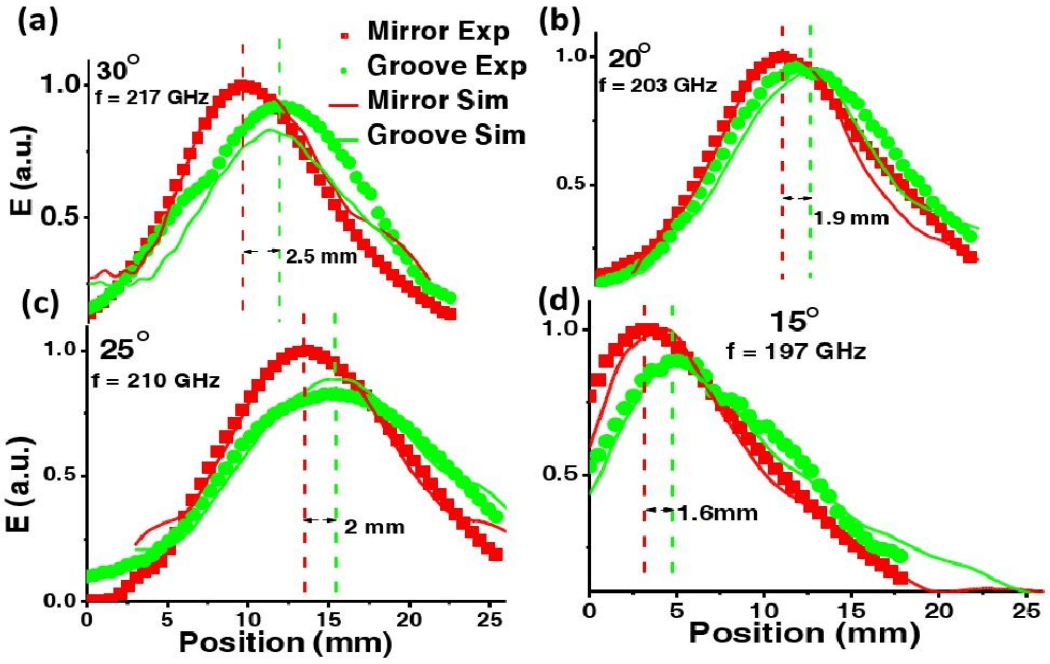

Figure 4.13 The lateral position shift of the reflected wave for different incident angles. Symbols (squares and circles) are for experimental data and solid lines are for simulated data (FEM).

The Figure 4.13 shows a typical resul of the lateral position shift Δ for four different incident angels. The mirror reflection signal is measured by pressing a aluminum mirror against the output facet of the waveguide, in comparison to the reflection by the groove patterns on output facet where no mirror in presence. For an

incident Gaussian beam of waist ~1.5 cm, we observed clear lateral shifts in the sacle of a few mm. This lateral shift increases as the angle of incidence increases. A FEM simulation confirms this spatial shift, as shown in solid lines in Figure 4.13. As noted previously [119], the magnitude of Δ is very generally related to the phase of the reflection coefficient according to:

$$\Delta = -\frac{1}{k}\frac{\partial \Phi}{\partial \theta}. \tag{4.9}$$

Substituting the expression of eq. (4.6) and (4.7) into (4.9), and simplifying the factors, we get the lateral shift as:

$$\Delta = \Delta_0 \sin(\theta) \tag{4.10}$$

where Δ_0 is a constant parameter related to the form of $\Phi(\kappa)$. Over the range of our angular measurements, this description is in good agreement with our observations (Fig. 14(a)).

Finally, associated with a Goos-Hänchen-like spatial shift, one also expects a phase shift between the wave reflected from a mirror and from the SSP reflection. From our measurements, we extract the frequency derivative of the spectral phase difference between sample and reference measurements, in order to express the result as a time shift for each angle θ. Our model predicts that this time shift should be given by [119]:

$$\delta t = \frac{\partial \Phi}{\partial \omega} = \delta t_0 \cos(\theta). \tag{4.11}$$

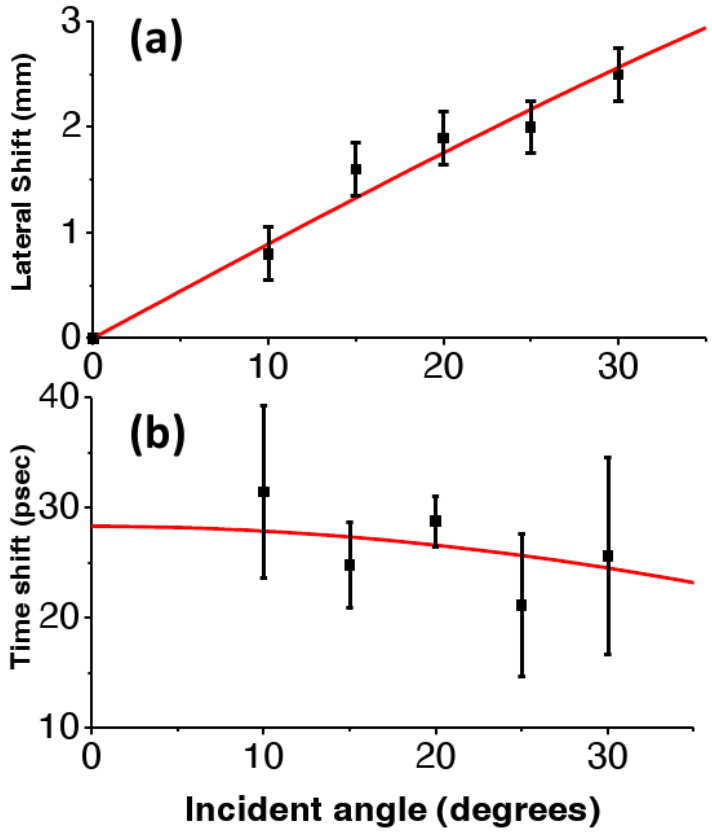

Figure 4.14 . (a) The lateral shift of the beam as a function of angle of incidence. The solid red curve is a plot of Eq. (4.10) with one fit parameter. (b) The temporal shift of the reflected beam (relative to that of a mirror reflection) as a function of angle of incidence. The solid red curve is a plot of Eq. (4.11) with no adjustable parameters.

Here δt_0 is the time shift at normal incidence, which can be extracted from the temporal waveforms used to create Fig. 4.10. With no fit parameters, this prediction is consistent with the time shifts extracted from the angle-dependent measurements, as shown in Fig. 4.14 (b).

4.4. A Prototype of a THz Band-pass resonator

Narrow-band resonators or filters have always been an interesting research area in the THz range, because of their applications in many areas of THz technologies, such as in wireless communications [120] and sensing[121, 122]. A few methods have been used to implement THz resonators, including quasi-optic resonators based on a Fabry-Perot cavity [122, 123], membrane resonators using metamaterials [124], wire-disk resonators which rely on whispering gallery modes [125], integrated waveguide-coupled THz resonators using microcavities [52, 126, 127], and Bragg gratings with defects [66, 121, 128]. In this part, I demonstrate a prototype of a band-pass THz resonator by using the concept of a designer reflector.

When a broadband THz wave is reflected at the output facet of a PPWG with an engineered groove pattern, it carries almost 100% of the energy at the design frequency (Fig. 4.10). Thus the patterned output surface acts as a nearly ideal THz filter, with a full width at half maximum (FWHM) of a few tens of GHz. Cascading of this filter operation will therefore lead to narrowing of the spectrum reflected back into the waveguide, with relatively little loss at the design frequency. Therefore, multiple reflections can be used to design a resonator with a high quality-factor Q and relatively high throughput.

To explore this concept, we first conduct FEM simulations of a structure in which the THz wave reflects three times off of a patterned facet. Fig. 4.15 illustrates

top-down views of the results of these simulations. These results display the electric field distributions when the THz beam is incident at an angle of 10° to the normal of the reflecting surfaces. The blue lines indicate the surfaces that are patterned with grooves to provide enhanced reflection. Fig. 4.15 (a) shows the result at the design frequency (174 GHz), while Fig. 4.15 (b) shows the same result except that the grooved surfaces have been replaced in the simulations by perfectly reflecting mirrors at the same locations. For these two cases, we observe that nearly the same energy is delivered to the output port of the device. Figures 4.15 (c) and 4.15 (d) show the results when the device is excited off resonance. The energy delivered to the output port drops to nearly zero for 160 GHz [Fig. 4.15 (c)] and 190 GHz [Fig. 4.15(d)].

When using a resonator based on the geometry shown in Fig. 4.15, the requirement of two identical groove patterns on both of the reflecting facets poses somewhat of a fabrication challenge. Typical machining tolerances of ~25 μm will lead to uncertainty in the groove geometrical parameters (L, h, and d), which will lead to shifts in the peak frequency for one reflecting surface relative to the other one. Obviously, in order for the resonator to operate as anticipated, such shifts are not desirable. Even a small difference in design frequency of less than 10 GHz will lead to a dramatic reshaping of the spectrum of the radiation reaching the output port, especially in the case of a large number of internal reflections.

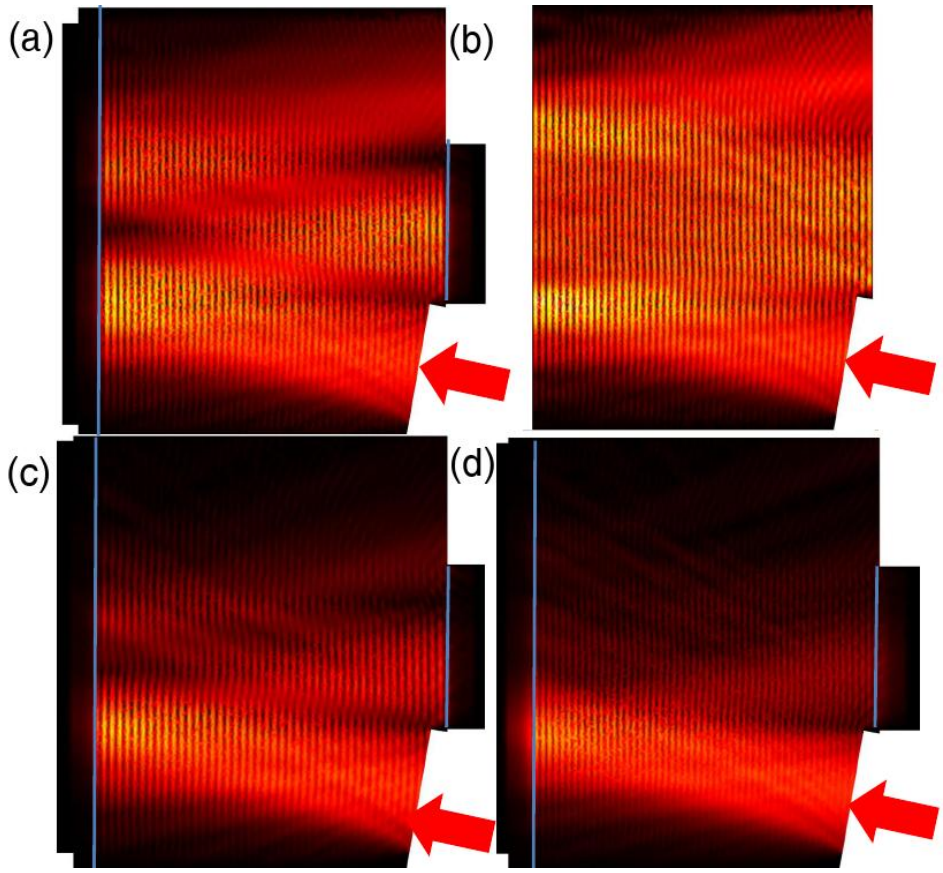

Figure 4.15 Plots of the electric field distribution (from 3D FEM simulations) inside the devices designed as resonators, with three internal reflections. (a) Device with the same pattern of grooves on both reflecting facets (marked by blue lines) when the input wave is at design frequency (174 GHz). (b) Device with perfect mirrors instead of the groove patterns, at the design frequency. (c) The same device as (a) except the input wave is at frequency 160 GHz. (d) The same device as (a) except the input wave is at frequency 190 GHz.

To avoid this problem, we modify the design for the THz resonator as shown in Fig. 4.16. Here, only one facet of the waveguide is decorated with grooves, while the other facet relies on a broadband mirror reflection. This firmly contacted mirror makes a perfect reflection at its interface for the THz waves coming from inside the

waveguide, creating an image of the groove-patterned facet symmetric to the mirror (as labeled in Fig. 4.16). The grooved surface has a length of 15 cm, in order to allow space for multiple reflections between the input and output port. The mirror on the upper facet can be lengthened or shortened, in order to control the number of internal reflections --- a longer mirror will give rise to more reflections before the wave reaches a point where it can escape from the device. Therefore the overall result is equivalent to reflection from two identical patterned facets as in Fig. 4.15, but without the fabrication challenge of creating two identical groove patterns on two different surfaces.

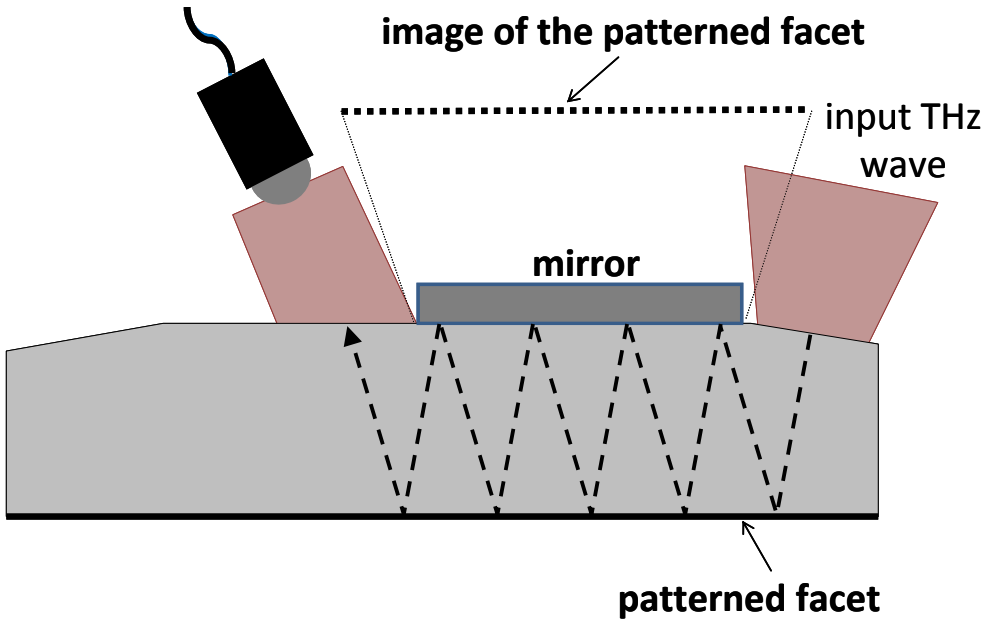

Figure 4.16 A schematic of the device with a single patterned facet, fabricated for the experimental measurements. The dotted line shows the image of the patterned facet. The dashed line shows a ray path of a multiply reflected THz beam inside the device.

To demonstrate this resonator, we fabricated the device as shown in Fig. 4.16. The groove pattern was designed for a peak frequency of 170 GHz when illuminated at normal incidence, or 167 GHz when illuminated at 10° (as is relevant here). The receiver is placed 2 cm away from the facet without a groove pattern, adjacent to the contact mirror, to collect the waves emerging from the waveguide. By varying the length of the reflecting mirror and adjusting the location of the receiver, the number of reflections on the patterned facet can be modified and identified in the time domain, since each subsequent reflection adds additional travel path length (and therefore time delay) to the signal. For each measurement, we acquire a reference signal by pressing another mirror tightly against the facet with groove patterns, similar to the procedure used for referencing for the data of Fig. 4.10.

The results of these measurements are shown in Fig. 4.17. A few typical output spectra are shown, for different numbers of internal reflections. Evidently, the width of the spectral peak decreases as the number of bounces increases, while the peak amplitude only changes by a small amount. We find that the FWHM decreases from ~30 GHz for the case of only one reflection to ~7 GHz for twelve reflections. We can understand this line narrowing as a simple cascading filter effect, as discussed above. To confirm this interpretation, we use the spectrum measured after a single reflection as a starting point, and compute the evolution of the FWHM by considering higher-order multiples of this spectrum. This result is

shown as the blue curve in the inset of Fig. 4.17, along with the measured widths (data points). These results are also consistent with numerical simulations (red curve).

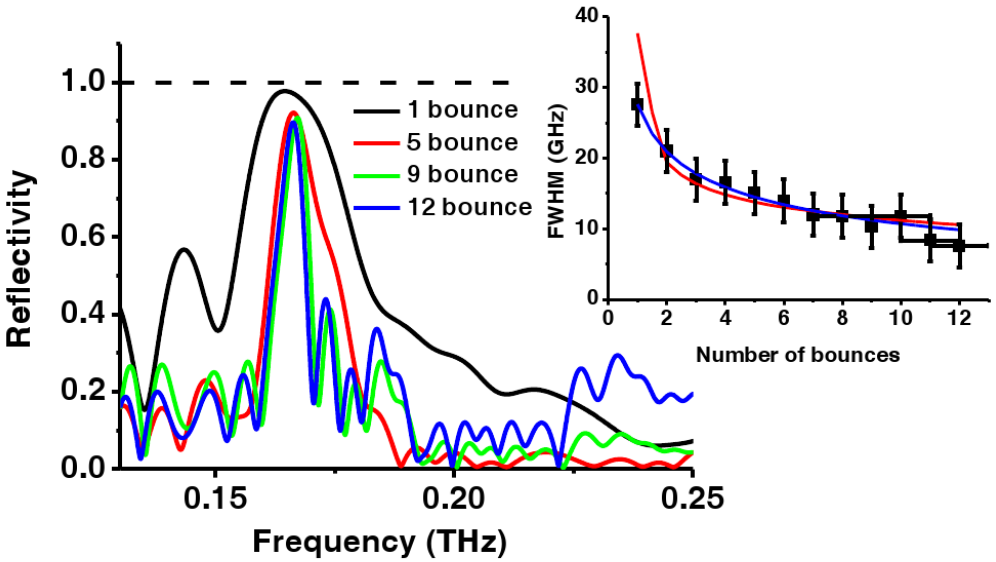

Figure 4.17 Normalized reflection spectra for the signals after multiple bounces inside the resonator device depicted in Fig. 4.16. The inset shows the full-width-at-half-maximum of the spectra as a function of the number of internal bounces off of the groove-patterned surface. The red curve shows the FEM simulation, while the blue curve shows a simple calculation extrapolating the line narrowing from the result from a single bounce. The black squares show the experimental results with estimated error bars.

It is important to note the effects of diffraction. The THz wave is coupled into a PPWG at a beam width of 1.5 cm using a pair of confocal lenses. The path length of the THz wave inside the waveguide after twelve bounces is almost 70 cm. Assuming Gaussian beam diffraction, we would expect a beam waist of ~9 cm at the output

port. Thus, for a large number of reflections, the signal collected at the receiver is actually an overlapping mix of several temporal signals that have experienced differing numbers of reflections. These are reasonably well separated in the time domain because each has traveled a different path length. However, since the filtering effect significantly stretches the original single-cycle pulse in the time domain, the trailing part of one particular reflection can overlap with the leading part of the subsequent reflection. This is essentially an experimental artifact of studying a narrowband effect using a broadband-pulse technology, which leads to some uncertainty in the extraction of, e.g., the precise linewidths (as shown by the error bars in Fig. 4.17). We would anticipate that this concern would be largely eliminated if a narrowband tunable THz source were used.

In conclusion, we have demonstrated that the reflectivity at the output facet of a PPWG can be enhanced almost up to 100% by using spoof surface plasmons. We presented a prototype of a THz resonator. This concept could be useful in a range of applications in THz technologies.

Chapter 5

Two-Dimensional Artificial Dielectric: A THz mirage Device

5.1. A THz mirage Device

The works in this section are achieved in cooperation with Dr. Rajind Mendis, who is the major contributor to this project, and Professor Daniel Mittleman. The author of this thesis contributed to all the 2D and 3D simulations, and participated in the project discussion.

The concept of waveguide-based artificial dielectrics had been studied half a century ago in the microwave community, but did not become popular for its unreasonably large size and therefore bulky volume for practical use [58]. However this concept is in a manageable size in THz range due to the wavelength scaling. In

this section we discuss the use of this concept to manipulate the beam propagation in the waveguide in a designed manner, such as beam bending and a mirage effect[14].

As we discussed in the introduction, the effective in the of a PPWG in TE1 mode is given by,

$$n_{eff} = \sqrt{1-(\frac{c}{2bf})^2} \tag{5.1}$$

where b is the plate separation, f is the frequency, and c is the free-space speed of light. This indicates that when the wave is at a fixed frequency, the index n_{eff} can be tuned between zeros and unity by changing the plate separation b.

In order to validate this concept, we first use a simple example where the index of refraction changes monotonically a long a single direction. This can be implemented simply by tilting one metal plate of a parallel-plate waveguide against the other. The variation of the plate separation creates an index gradient in the medium, which leads to the bending of the light rays toward the high index region, in a principle similar to Snell's law. In the context of the waveguide-based medium, the region of a larger plate separation has a higher index. Therefore, we expect the THz beam propagating in the waveguide to bend towards the regions of larger plate spacing.

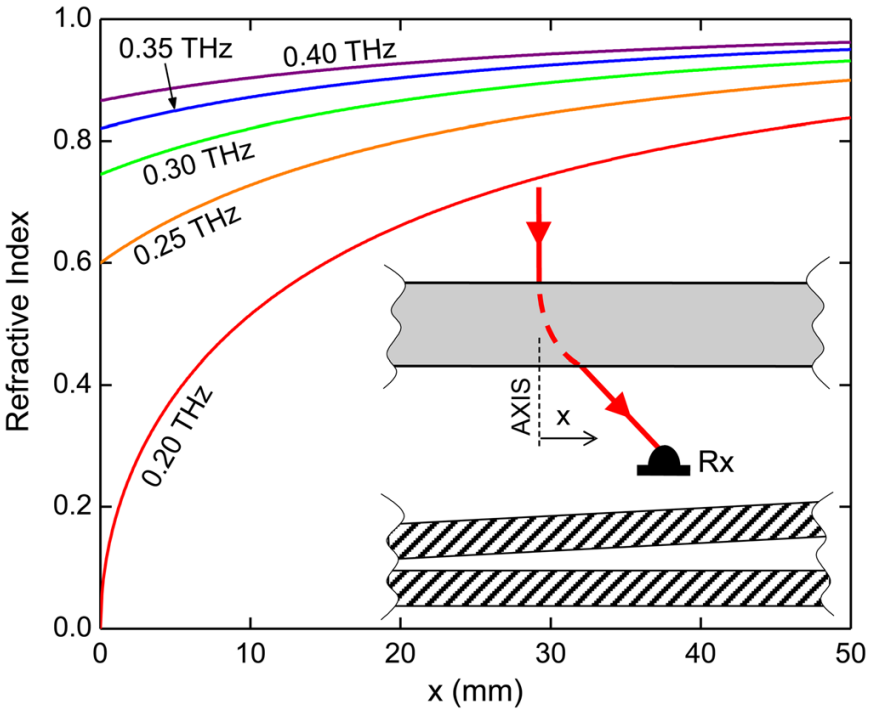

Figure 5.1 (Extracted from [14]) The calculated refractive index as a function of x coordinate for several different frequencies. The inset shows the schematic of the waveguide in the experiment. The red curve shows the trace of a THz beam bending toward higher plate separation.

For the experiment, we chose a PPWG of length 1 cm, which has the top plate tilted in a way that the plate separation increases along the width of the waveguide (Inset of Figure 5.1). The angle θ between the top plate and bottom plate is 0.72°. A broad-band THz wave is coupled into the waveguide at normal incidence. In order to excite the TE1 mode, the polarization of the THz wave is parallel to the bottom plate. We set the position of the input optic axis as a reference (x = 0), at which the plate separation is 0.75 mm (In set of Figure 5.1). By using the definition of the effective index of refraction, we calculate the index profile as a function of transverse coordinate (x) for five different frequencies (Figure 5.1). These curves indicate that for a given waveguide, the effective index of refraction has fewer

gradients for low frequencies, which lead to stronger level of beam bending for waves at low frequencies. Thus for a broad-band input beam, the components of lower frequencies experience more index gradients, and then get greater deflections than these of higher frequencies. We scanned the THz receiver along x axis at a distance 3 cm away from the output face of the waveguide (Figure 5.1 Inset). At different positions, the received signals by the receiver have different spectra, as indicated in figure 5.2. As we expected, the components of the low frequencies (red curve) is deflected away (x = 24mm) from the optical axis (x = 0), and therefore not shown up in the signal measured on the optical axis (black curve). As the receiver moves away from the optical axis, we observe a continuous increase of wave components at lower frequencies. By extracting the spectral amplitude of the signals at each position of x axis, we plot the spatial intensity profile of the output beam for different frequencies (Figure 5.3). For comparison, we also plot the spatial intensity profile for the case the waveguide has two metal plates parallel to each other (black curve). As shown in figure 5.3, the back curve shows a Gaussian shape centered at x = 0 while the red curve shows a shift off the axis x = 0. The amount of this shift increases as the frequencies decreases. We must note that the frequency components have a lower limit, which is the cut-off frequency of the waveguide determined by the plate separation at the input location. For this case, the cut off frequency is 200 GHz (b = 0.75 mm at x = 0).

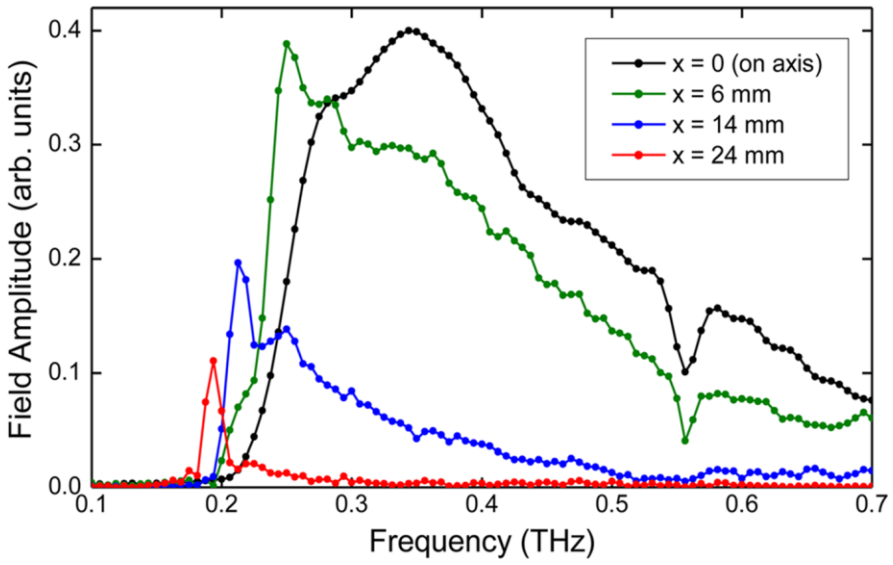

Figure 5.2 (Extracted from [14]) The spectrum of the measured signals at different positions on the x axis. X = 0 corresponds to the optical axis of the input beam. The positive x is in the direction along which the plate spacing increases.

In this simple case, a waveguide with a tilted top plate is able to bend the wave propagation in TE1 mode in the empty space between the two plates, as if it were a dielectric with a gradient of refractive index. On the basis of this beam bending, more sophisticated designs become possible to control the beam propagation inside a waveguide. In this project, we demonstrate a device which bends a light around an obstructing object. This is the essence of a mirage, so the device is also called a THz mirage device.

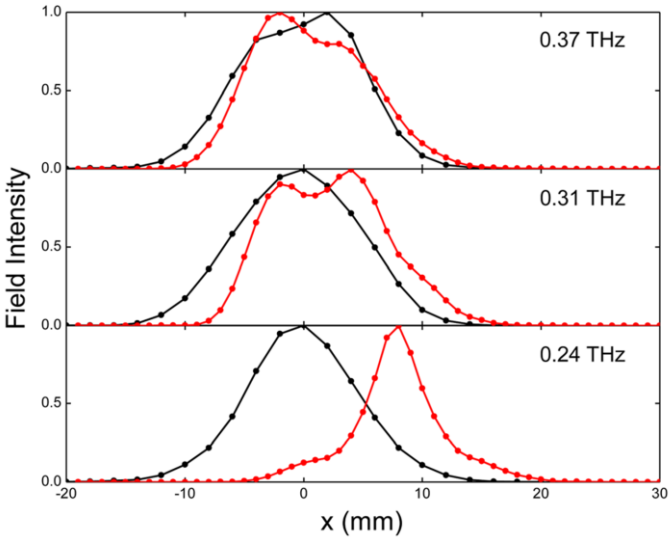

Figure 5.3 (Extracted from [14]) The distribution of electric field amplitude along the x axis for different frequencies. The red curves are for the waveguide with a tilted top plate. The black curves are for the PPWG with parallel plates.

To manipulate the light wave around an object, we have to first bend it in a direction in front of the object, to avoid the interaction with the object, and then steer it back after it passes the object. This process involves bending the beam twice in opposite direction. The deflection of the light wave in the waveguide is essentially a result of the index gradient, which makes the beam propagate toward the region of higher index. A prescription to steer the light beam consecutively in opposite direction is to put two symmetric regions together with respect to a mirror plane. The two regions have the same geometries but opposite directions of index gradients, as indicated in figure 5.4. These opposite index gradients guide the light

waves around an area in the middle of the waveguide, no matter what material this area is made of.

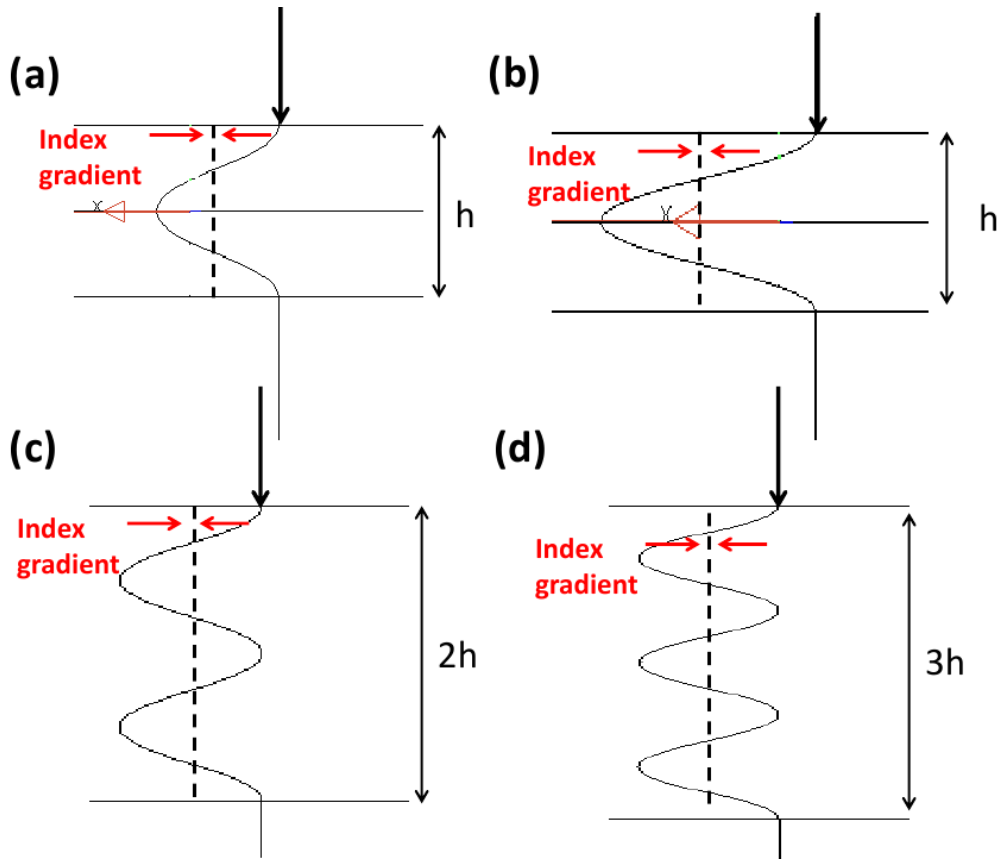

Figure 5.4 The ray trace simulation of the mirage device design. The input beam in coupled into the device at normal incidence. (a) A design making beam propagate around an area in the middle of waveguide. (b) The similar design to (a), except the position of the input beam and the mirror plane is difference. (c) A design of light wave moving around two consecutive areas in the same waveguide. (d) A design of light moving around three areas in the same waveguide.

To exploit this prescription, we conducted numerical simulations for the devices with same index gradient but different geometries, mirror plane locations and the positions of the input beam, as indicated in figure 5.4. The simulation is based on a ray tracing method (LightTools), and the index of refraction can be set as a property of the medium in the simulation. In figure 5.4 (a), the waveguide has a length of 5 cm (h) with the input beam 3.6 cm away from the mirror plane. We observe that by finely tune the position of the input beam and the mirror plane, the light waves can be guided around an object of the size comparable to the waveguide, and steered back to propagate in the same direction as the input beam. Furthermore by changing the position of the input beam and the mirror plane, we can engineer the trace of the beam propagation inside the waveguide, as implied by another example in figure 5.4 (b). This prescription can be implemented further by extending the length of the waveguide. In figure 5.4 (c) and (d), the light waves were guided around two and three consecutive objects respectively, by simply extending the length of the waveguide in figure 5.4(a) by two and three times. However, these simulations are only based on ray tracing in two dimensions, which is an overly simplified model for the real three dimensional waveguide-based mirage device. For further investigation of the mirage device, we choose a simple design as shown in the example in figure 5.4(a).

The design in figure 5.4(a) is related to a “roof” structure in the waveguide-base artificial dielectric, where the upper waveguide plate has two complementary

flat inclined surfaces (Figure 5.5 (a)). The plate separation b varies as a function the transverse coordinate $b(x) = b_0 - m|x|$, where x = 0 corresponds to the position of mirror plane, b0 is the maximum plate separation, and m is the slope of the roof structure that determines the intensity of the index gradient. In the waveguide-based artificial dielectric, the index prescription only works for a single frequency. When a broad-band THz wave is coupled into the roof structure at the designed input location, the mirage device takes effect only for a single frequency component, which is used in the design (red curve in figure 5.5 (b)). If we put a circular metal structure in the middle of the waveguide, it casts shadows for the waves at other frequencies which do not pass around this area (blue curve in figure 5.5(b)).

By using finite element method, we perform a full three-dimensional numerical simulation of the mirage device. Figure 5.5 (c) shows the color-plot of a cross-section in a plane through the middle of the gap between the two plates. In this simulation, a cylindrical space in the middle of the waveguide, as indicated by a blue area in the figure, is set as metal block to emulate a metal obstruction (to be hidden). The curved trace of the normally incident light wave passes around the metal obstruction and emerges from the waveguide without casting any shadows. This is evidenced by figure 5.5 (d) and (e), which are the color plot of the electric field intensity at the output facet of the waveguide, with and without the metal block. No distinguishable shadow can be identified in the case of a metal block.

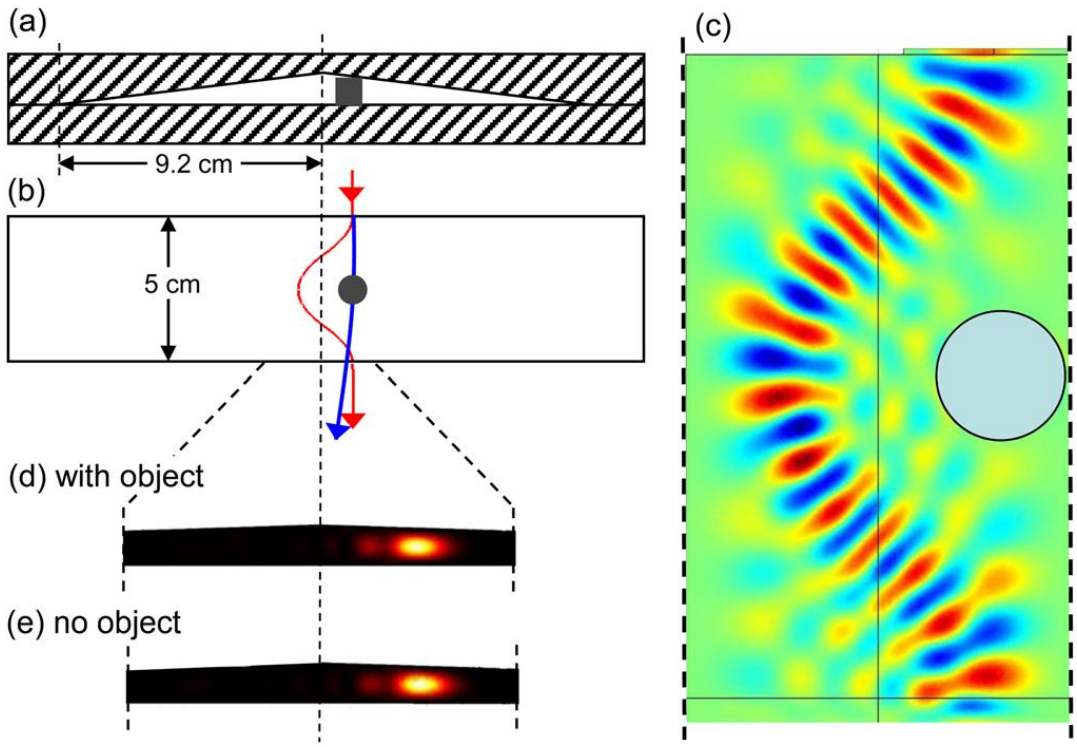

Figure 5.5 (Extracted from [14]) (a) The cross-sectional view of the waveguide showing the roof structure of the mirage device. (b) The ray traces of light propagation in the mirage device for frequency at 0.16 THz (red) and 0.54 THz (blue). (c) A full wave 3D simulation of the mirage device. (d) The intensity pattern at the output facet of the waveguide, with and without the metal obstruction in place.

We conduct an experiment to validate this mirage device. A length of the waveguide is 5 cm, the mirror plane (or the roof apex) is 9.2 cm away from the plate contact point is the transverse direction, and the inclination angle is 0.68°. The frequency in the mirage device design is 0.16 THz. The metal object is a cylindrical with a height of 0.8 mm and a radius of 5 mm. A broad-band THz wave is coupled into the waveguide at the designed input position. The THz receiver is scanned 3 cm

away from the output facet of the waveguide, on the x axis along the transverse direction. Two sets of data are measured: one is for the case with a metal object, one is same device without the object. The spatial profiles of the measured intensity are shown in figure 5.6 for two different frequencies, 0.16 THz and 0.54 THz. At the designed frequency (figure 5.6 (a)), we observe almost the same spatial profiles for the two cases, which imply that the object casts no shadow for the wave. At the frequency different from the designed one (figure 5.6 (b)), a very obvious shadow structure can be identified in the case with an object in presence.

In this section, we have demonstrated a new approach to creating an inhomogeneous artificial medium based on the TE1 mode of PPWG. The new approach can be used to bend the light propagation in the waveguide, as if it is in the real medium with the same index. We demonstrated a mirage device working at a single frequency, in which an object of size several times larger than the wavelength can be hide from the THz wave at the designed frequency.

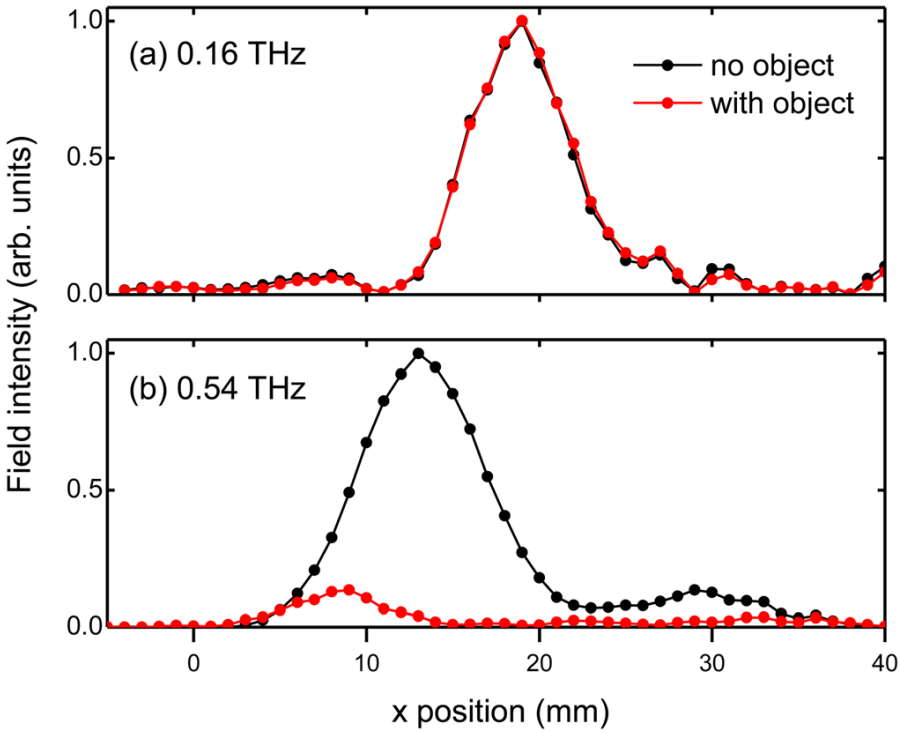

Figure 5.6 The spatial distribution of the electric field intensity in the experiment for a designed mirage device. (a) The intensity profile at the designed frequency 0.16 THz. (b) The intensity profile at a different frequency 0.54 THz. The black curves are for the case without an object, the red curves are for the case with an object in place.

Chapter 6:

Conclusions and Future Directions

6.1. Conclusions and Limits of The Novel Imaging Probe for The Broad-band THz Near-field Imaging

In Chapter 3, we discussed a tapered PPWG as a probe for the broad-band THz near-field imaging. This one-dimensionally-tapered-PPWG probe provides a good line illuminator with a high aspect ratio. The FBP algorithm is implemented to reconstruct the image from the measured signals of average wavelength of 1.5 mm. Features of ~ 100 μm can be resolved in the reconstructed image.

In this part, we investigated the resolution limit of this probe for near-field imaging by using finite-element method simulation. The tapered parallel-plate waveguide is an effective technique to deliver THz waves into small areas without

cut-off and dispersions [70-72]. In the imaging experiment, we tapered the spacing between the two metal plates from 1.5 mm at the input to 20 μm at the output. The reflection coefficient of the output interface is more than 90% for the THz waves in our experiment. For the same geometry, we simulated the reflection coefficient as a function of output spacing of the tapered PPWG (Figure 6.1 (a)). We observed that, for the same input spacing of 1.5 mm, the reflectivity increases with the decreases of the output spacing. And the reflectivity approaches to almost unity when the output is below 1 μm. Also we simulated the reflectivity as a function of the distance from an Aluminum sample to the imaging probe. Figure 6.1 (b) shows the relations for the imaging probes of different output sizes. Similar to probe of 20 μm output spacing shown in Figure 3.3, the reflectivity of the output interface drops as the Aluminum sample is moved away from the imaging probe. When the distance between the sample and probe increases beyond a certain distance (2 μm for a 200 nm probe), the reflectivity increases again and approaches to the reflectivity determined by the output spacing (Figure 6.1(a)). There is a distance at which the reflectivity reaches a dip, and it varies with the different output spacing. For the probe of output 80 nm, the dip happens when the sample is ~1 μm away from the aperture.

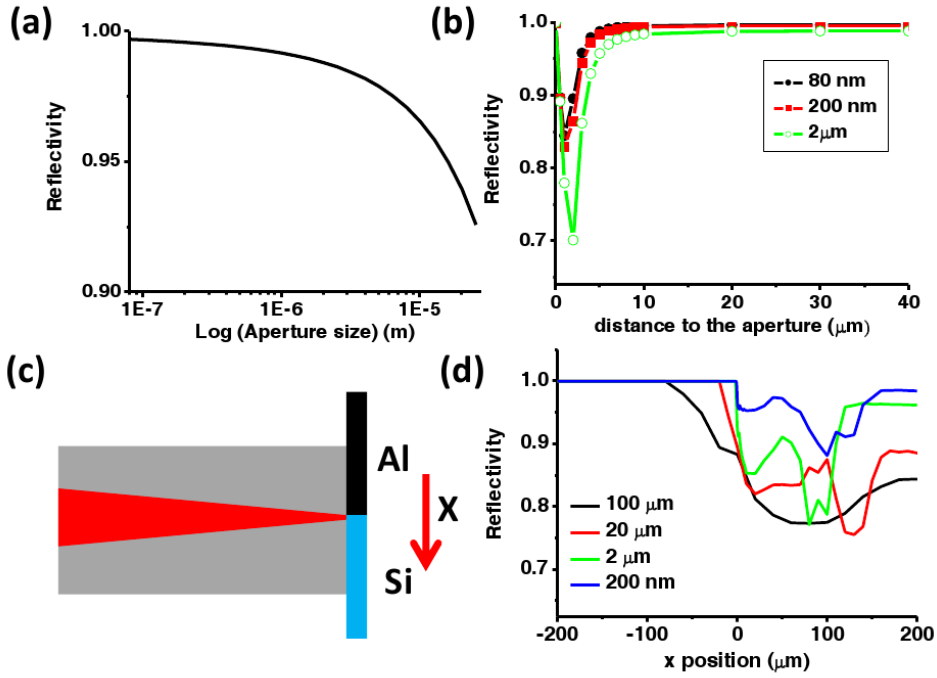

Figure 6.1 (a) Reflection coefficient of the tapered PPWG (tapered from 1.5 mm in the input) as a function of the output aperture size. (b) Reflection coefficient of Aluminum sample as a function of the distance to the probe output aperture. (c) Schematic of the imaging sample simulation. (d) The change of the reflectivity as the imaging sample scans across the imaging probe.

In another simulation, we put the sample in exact contact with the imaging probe. In this way, the near-field electromagnetic waves of the probe have the best interaction with the imaging samples, and therefore carry the most information of the imaging sample. To explore the limit of the imaging resolution, we simulated a typical case, in which the imaging sample consists of an aluminum part and a silicon part with a distinctive boundary between them (Figure 6.1 (c)). This sample is

scanned across the imaging probe in the simulations, which have the center of the probe at x = 0 μm. The reflectivity is plotted as a function of the scan position in figure 6.1 (d). When x is at the position of large negative coordinates (< -200 μm), the aluminum sample covers the entire imaging aperture, and therefore the reflectivity is unity. When x is at the position of large positive coordinates (> 200 μm), the silicon sample covers the entire imaging aperture. The reflectivity is then less than unity depending on the output spacing. For example, the reflectivity is more than 98% when the output is 200 nm (blue curve in Figure 6.1(d)). To have a good reconstructed image, the signals (reflection) of different imaging samples should have sufficient contrast, and the transitions between these two different signals should happen in a small region. The length of this small region determines the resolution of the reconstructed image. As we observed in Figure 6.1 (d), for the probe of size 100 μm, the Michelson contrast is relatively strong (1.0 - 0.8 /1.0 + 0.8~ 0.11); while for the probe of size 200 nm, the contrast is very week (1.0 – 0.98/1.0 + 0.98 ~ 0.01). In the simulation, a reflectivity drop is observed in the transition region, where the reflectivity has its minimum. Similar to the discussion in Chapter 3, this reflectivity drop can be explained by the impedance change of the waveguide structure as the boundary between the Al and the Si is scanned across the probe aperture. The width of the signal transition region doesn't decrease as the aperture size shrinks. In the case of 2 μm aperture size, the transition region is as wide as 100 μm. Therefore, even if we use the probe of 200 nm output spacing, the

resolution is also 100 μm without significant improvement compared to that reported in Chap 3, but the imaging contrast degrades 10 times.

In summary, we can improve the imaging resolution to some extent by the decrease of the probe aperture. However there is a limit of the resolution (~ 100 μm). When the image resolution reaches this limit, it can't be improved by reducing the output spacing of the imaging probe.

6.2. Conclusions and Future works for Spoof Surface Plasmon reflector and the Band-pass THz resonator

As we concluded in Chapter 4, we demonstrated that the reflectivity at the output facet of a PPWG can be enhanced almost up to 100% by using spoof surface plasmons. This enhancement works only for a single THz frequency. Also this reflectivity can be engineered in a range from 0% to almost 100%. This new technique is a good analogy of the coating techniques that are widely used in the optical device industry. Therefore it could have a wide range of applications in terahertz technologies, such as the input mirror for a THz cavity, and the frequency selective reflector for a THz ring-down spectrometer.

We presented a prototype of a THz resonator based on this new SSP reflector. This resonator could be further developed into a very sensitive THz gas sensor. Because the path length of the THz waves in such a small resonator is almost

70 cm, and the Q value of this resonator is also high, this device can be very sensitive to the gas that absorbs the THz waves at the working frequency.

To develop this gas sensor, a few challenges are expected. One is the fabrication challenge of the smaller groove patterns. For most common gases, the absorption peak in THz range is more than 500 GHz, such as water vapor at 556 GHz. This high frequency requires a significant scale-down of the groove pattern. And therefore the accurate fabrication of these groove patterns is more expensive in terms of time and cost. Another challenge comes with the diffraction of the THz waves. As the input THz wave has a beam width of 1 cm, it should have a significant diffraction after it propagates a path of more than 70 cm in the device. To overcome this diffraction, we may resort to some traditional techniques. For example, we could replace the Aluminum mirror with a curved reflection interface (shown in Figure 4.16). The curvature of the interface is designed to compensate the diffraction of the THz wave for each round-trip in the device. Therefore these challenges are not the fundamental barrier and can be solved at a reasonable cost in the near future.

6.3. Conclusions and Preliminary Results for the Two-Dimensional Maxwell's fish eye

In Chapter 5, we have demonstrated a new approach to creating an inhomogeneous artificial medium based on the TE1 mode of the PPWG. The new approach is able to bend the light propagation in the waveguide, as if it is in the real medium with the same index. We demonstrated a mirage device working at a single frequency, in which an object several times larger than the wavelength can be hid from the THz wave at the designed frequency.

The concept of the 2D inhomogeneous artificial dielectric opens up numerous possibilities to manipulate terahertz wave in a two dimensional space, which is comparable to a two dimensional version of the widely studied matamaterials. The differences are that the 2D inhomogeneous artificial dielectric works in the TE1 mode of a waveguide, and the dielectric properties can be engineered in an ideally continuous way as that in the mirage device.

The significance of this work is leveraged by two emerging disciplines. One is the transformation optics, which is inspired by the invention of the matamaterials. The transformation optics is the basis for conceptualizing complex tools for novel control of light. Thus it is a powerful theoretical tool box, in which there are many prescriptions of novel optical devices. Some of these fantastic prescriptions for the novel devices can be translated into a 2D version and be implemented by the 2D

inhomogeneous artificial dielectric. Another emerging discipline is the high resolution 3D printing technologies, which make it possible and affordable to fabricate a waveguide with complex features that meets the requirement of the prescription.

In this part, we show a demonstration of a 2D Maxwell's fish eye. This is a good example to illustrate the power of this 2D artificial dielectric combined with the high resolution 3D printing technologies.

The Maxwell's fish eye is a spherically symmetric lens, with a refractive index that varies from the center to the outer boundary. This type of lenses has an unusual ability to focus the beams emitted by a point source at one edge to another point on the opposite side of the lens. The refractive index is prescribed as $n = n0/(1+(r/R)^2)$, where n_0 is a positive constant and R is the radius of the lens. After translating into our 2D dielectric, the plate separation of the waveguide is represented by the following equation.

$$b = \frac{\lambda}{2}\frac{1}{\sqrt{1-(\frac{n0}{1+\left(\frac{r}{R}\right)^2})^2}} \qquad (6.1)$$

Where b is the plate spacing between the waveguide, λ is the wavelength, r is the distance to the center, and R is the radius of the device. We chose the working

frequency as 150 GHz, which corresponds to a wavelength of 2 mm. The profile of equation (6.1) is plotted in Figure 6.2 (a). In order to accurately fabricate the waveguide, we choose a flat bottom plate and a curved top plate with the curvature according to equation (6.1). The effectiveness of this 2D Maxwell's fish eye is shown in Figure 6.2 (b) by a FEM simulation.

The fabrication of the top plate of the waveguide is very challenging for the traditional machine shop, because the curvature of top plate is in a complex functional form (equation 6.1). We chose the high resolution 3D printing technique, which has a resolution of 20 μm. Compared to the working wavelength of 2 mm, this finite resolution can be ignored and the curve is considered as continuous. The profile of the print-out from the 3D printing shows a very good match to the designed profile (Figure 6.3 (a).). However, the 3D print-out is made of plastic, so we coated the curved surface by a high conductive metallic paint. The preliminary experimental results are shown in Figure 6.3 (b). We observed that when the fish eye is excited on one side by a point source, the beam at the designed frequency is focused to a point on the other side. For the beams at other frequencies, they experienced a large diffraction by going through the narrow input aperture.

The detailed discussions of the Maxwell's fish eye and the full appreciation of the significance of the 2D inhomogeneous artificial dielectric are beyond the scope

of this thesis. The most recent reports can be found in the publications from Mittleman Group in Rice University.

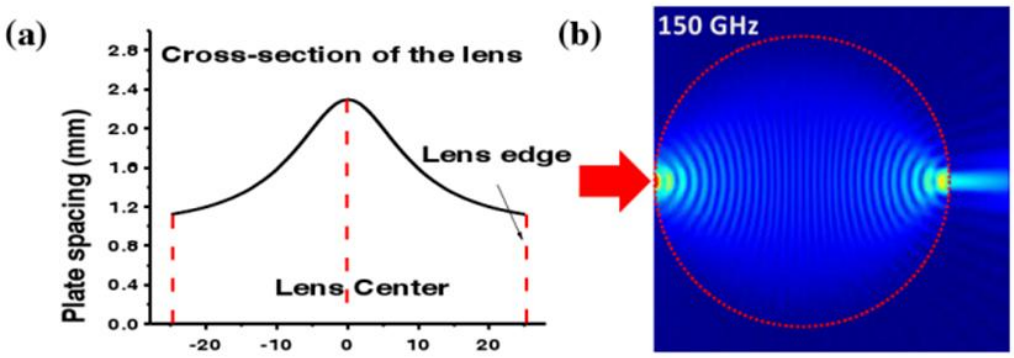

Figure 6.2 (a) The plate separation of the waveguide as a function of the distance to the center. (b) The FEM simulation of the two dimensional Maxwell's fish eye.

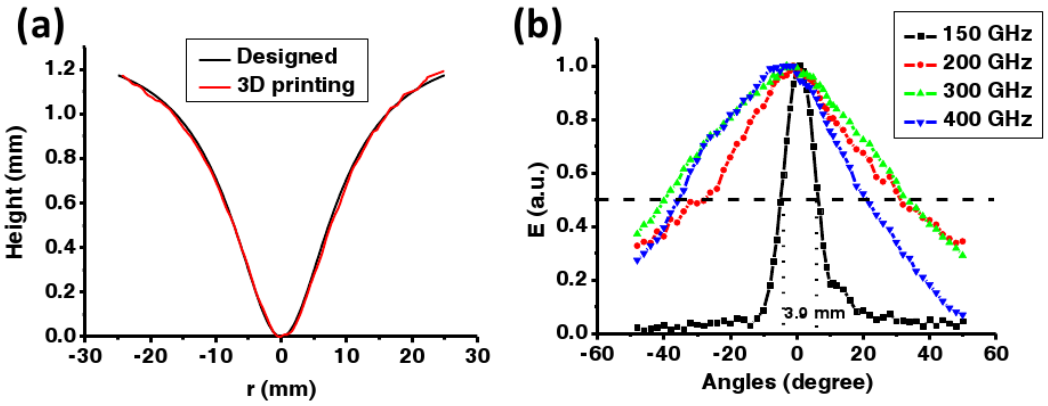

Figure 6.3 (a) A comparison of the curve profile of top plate of the 2D Maxwell's fish eye between the designed profile and the fabricated from 3D printing. (b) The experimentally measured beam focusing at the designed frequency.

References

[1] B. B. Hu and M. C. Nuss, "Imaging with terahertz waves," *Opt. Lett.,* vol. 20, pp. 1716-1718, 1995.

[2] M. Y. Glyavin, A. G. Luchinin, and G. Y. Golubiatnikov, "Generation of 1.5-kW, 1-THz Coherent Radiation from a Gyrotron with a Pulsed Magnetic Field," *Physical Review Letters,* vol. 100, p. 015101, 2008.

[3] A. Dobroiu, M. Yamashita, Y. N. Ohshima, Y. Morita, C. Otani, and K. Kawase, "Terahertz Imaging System Based on a Backward-Wave Oscillator," *Appl. Opt.,* vol. 43, pp. 5637-5646, 2004.

[4] J. Farhoomand and H. Pickett, "Stable 1.25 watts CW far infrared laser radiation at the 119 μm methanol line," *International Journal of Infrared and Millimeter Waves,* vol. 8, pp. 441-447, 1987/05/01 1987.

[5] B. S. Williams, "Terahertz quantum-cascade lasers," *Nat Photon,* vol. 1, pp. 517-525, 2007.

[6] M. Nuss and J. Orenstein, "Terahertz time-domain spectroscopy," in *Millimeter and Submillimeter Wave Spectroscopy of Solids*. vol. 74, G. Grüner, Ed., ed: Springer Berlin Heidelberg, 1998, pp. 7-50.

[7] M. Asada, S. Suzuki, and N. Kishimoto, "Resonant Tunneling Diodes for Sub-Terahertz and Terahertz Oscillators," *Japanese Journal of Applied Physics,* vol. 47, p. 4375.

[8] F. S. Yu C, Sun Y, Pickwell-Macpherson E, "The potential of terahertz imaging for cancer diagnosis: A review of investigations to date," *Quant Imaging Med Surg,* vol. 2, pp. 33-45, 2012.

[9] L. C. Crawley D, Wallace VP, Cole B, Arnone D, Pepper M., "Three-dimensional terahertz pulse imaging of dental tissue," *J Biomed Opt. ,* vol. 8, p. 303, 2003.

[10] A. D. B. A. Giles Davies, Wenhui Fan, Edmund H. Linfield, and John E. Cunningham, "Terahertz spectroscopy of explosives and drugs," *Materials Today,* vol. 11, 2008.

[11] D. M. (Ed.), *Sensing with Terahertz Radiations*. New York: Springer, 2003.

[12] K. Ishigaki, M. Shiraishi, S. Suzuki, M. Asada, N. Nishiyama, and S. Arai, "Direct intensity modulation and wireless data transmission characteristics of terahertz-oscillating resonant tunnelling diodes," *Electronics Letters,* vol. 48, pp. 582-583, 2012.

[13] N. Yu, Q. J. Wang, M. A. Kats, J. A. Fan, F. Capasso, S. P. Khanna, L. Li, A. G. Davies, and E. H. Linfield, "Terahertz plasmonics," *Electronics Letters,* vol. 46, pp. s52-s57, 2010.

[14] R. Mendis, J. Liu, and D. M. Mittleman, "Terahertz mirage: Deflecting terahertz beams in an inhomogeneous artificial dielectric based on a parallel-plate waveguide," *Applied Physics Letters,* vol. 101, p. 111108, 2012.

[15] R. Mendis, A. Nag, F. Chen, and D. M. Mittleman, "A tunable universal terahertz filter using artificial dielectrics based on parallel-plate waveguides," *Applied Physics Letters,* vol. 97, p. 131106, 2010.
[16] R. Mendis and D. M. Mittleman, "An investigation of the lowest-order transverse-electric (TE1) mode of the parallel-plate waveguide for THz pulse propagation," *J. Opt. Soc. Am. B,* vol. 26, pp. A6-A13, 2009.
[17] R. Mendis and D. M. Mittleman, "Comparison of the lowest-order transverse-electric (TE1) and transverse-magnetic (TEM) modes of the parallel-plate waveguide for terahertz pulse applications," *Opt. Express,* vol. 17, pp. 14839-14850, 2009.
[18] N. Marcuvitz, *Waveguide Handbook*. London, United Kingdom: The institution of Engineering and Technology, 1986.
[19] R. Mendis and D. Grischkowsky, "Undistorted guided-wave propagation of subpicosecond terahertz pulses," *Opt. Lett.,* vol. 26, p. 846, 2001.
[20] D. M. Mittleman, R. H. Jacobsen, and M. C. Nuss, "T-ray imaging," *Selected Topics in Quantum Electronics, IEEE Journal of,* vol. 2, pp. 679-692, 1996.
[21] J. Chen, Y. Chen, H. Zhao, G. J. Bastiaans, and X. C. Zhang, "Absorption coefficients of selected explosives and related compounds in the range of 0.1-2.8 THz," *Opt. Express,* vol. 15, pp. 12060-12067, 2007.
[22] D. M. Mittleman, M. Gupta, R. Neelamani, R. G. Baraniuk, J. V. Rudd, and M. Koch, "Recent advances in terahertz imaging," *Applied Physics B,* vol. 68, pp. 1085-1094, 1999/06/01 1999.
[23] J. D. a. D. M. Wai Lam Chan, "Imaging with terahertz radiation," *Rep. Prog. Phys.,* vol. 70, p. 1325, 2007.
[24] S. Hunsche, M. Koch, I. Brener, and M. C. Nuss, "THz near-field imaging," *Optics Communications,* vol. 150, pp. 22-26, 1998.
[25] D. M. M. S. Hunsche, M. Koch, and M. C. Nuss, "New dimensions in T-Ray Imaging," *IEICE Trans. Electron,* vol. 81-C(2), pp. 269-276, 1998.
[26] H. A. Bethe, "Theory of Diffraction by Small Holes," *Physical Review,* vol. 66, pp. 163-182, 1944.
[27] O. Mitrofanov, M. Lee, J. W. P. Hsu, L. N. Pfeiffer, K. W. West, J. D. Wynn, and J. F. Federici, "Terahertz pulse propagation through small apertures," *Applied Physics Letters,* vol. 79, pp. 907-909, 2001.
[28] A. Nahata and T. F. Heinz, "Reshaping of freely propagating terahertz pulses by diffraction," *Selected Topics in Quantum Electronics, IEEE Journal of,* vol. 2, pp. 701-708, 1996.
[29] R. W. McGowan, G. Gallot, and D. Grischkowsky, "Propagation of ultrawideband short pulses of terahertz radiation through submillimeter-diameter circular waveguides," *Opt. Lett.,* vol. 24, pp. 1431-1433, 1999.
[30] K. Ishihara, K. Ohashi, T. Ikari, H. Minamide, H. Yokoyama, J.-i. Shikata, and H. Ito, "Terahertz-wave near-field imaging with subwavelength resolution using

surface-wave-assisted bow-tie aperture," *Applied Physics Letters,* vol. 89, p. 201120, 2006.
[31] U. Schade, K. Holldack, P. Kuske, G. Wustefeld, and H.-W. Hubers, "THz near-field imaging employing synchrotron radiation," *Applied Physics Letters,* vol. 84, pp. 1422-1424, 2004.
[32] N. C. J. v. d. Valk and P. C. M. Planken, "Electro-optic detection of subwavelength terahertz spot sizes in the near field of a metal tip," *Applied Physics Letters,* vol. 81, pp. 1558-1560, 2002.
[33] H.-T. Chen, R. Kersting, and G. C. Cho, "Terahertz imaging with nanometer resolution," *Applied Physics Letters,* vol. 83, pp. 3009-3011, 2003.
[34] K. Wang, A. Barkan, and D. M. Mittleman, "Propagation effects in apertureless near-field optical antennas," *Applied Physics Letters,* vol. 84, pp. 305-307, 2004.
[35] K. Wang, D. M. Mittleman, N. C. J. v. d. Valk, and P. C. M. Planken, "Antenna effects in terahertz apertureless near-field optical microscopy," *Applied Physics Letters,* vol. 85, pp. 2715-2717, 2004.
[36] J. Zenneck, "U¨ ber die Fortpflanzung ebener elektromagnetischer Wellen la¨ngs einer ebenen Leiterfla¨che und ihre Beziehung zur drahtlosen Telegraphie," *Ann. Phys.,* vol. 23, pp. 846-866, 1907.
[37] A. D. a. T. a. E. W. Barnes, "Surface plasmon subwavelength optics," *Nature,* vol. 424, pp. 824-830, 2003.
[38] E. Ozbay, "Plasmonics: Merging photonics and electronics at nanoscale dimensions," *Science,* vol. 311, pp. 189-193, 2006.
[39] H. Atwater, "The promise of plasmonics," *Sci. Am.,* vol. 296, p. 4, 2007.
[40] T.-I. Jeon and D. Grischkowsky, "THz Zenneck surface wave (THz surface plasmon) propagation on a metal sheet," *Applied Physics Letters,* vol. 88, p. 061113, 2006.
[41] J. Saxler, J. Gómez Rivas, C. Janke, H. P. M. Pellemans, P. H. Bolívar, and H. Kurz, "Time-domain measurements of surface plasmon polaritons in the terahertz frequency range," *Physical Review B,* vol. 69, p. 155427, 2004.
[42] A. D. Boardman, *Electromagnetic surface modes*. New York: Wiley, 1982.
[43] R. H., *Surface Plasmons on smooth and rough surfaces and on gratings*. Berlin: Springer, 1988.
[44] S. A. Maier, S. R. Andrews, L. Martin-Moreno, and F. J. Garcia-Vidal, "Terahertz surface plasmon-polariton propagation and focusing on periodically corrugated metal wires," *Phys. Rev. Lett.,* vol. 97, p. 176805, 2006.
[45] N. Yu, Q. J. Wang, M. A. Kats, J. A. Fan, S. P. Khanna, L. H. Li, A. G. Davies, E. H. Linfield, and F. Capasso, "Designer spoof surface plasmon structures collimate terahertz laser beams," *Nat. Mater.,* vol. 9, pp. 730-735, 2010.
[46] A. Sommerfeld, "U" ber die Ausbreitung der Wellen in der drahtlosen Telegraphie," *Ann. Phys.,* vol. 28, pp. 665-736, 1909.

[47] H. Cao, R. A. Linke, and A. Nahata, "Broadband generation of terahertz radiation in a waveguide," *Opt. Lett.,* vol. 29, pp. 1751-1753, 2004.
[48] J. Zhang and D. Grischkowsky, "Waveguide terahertz time-domain spectroscopy of nanometer water layers," *Opt. Lett.,* vol. 29, pp. 1617-1619, 2004.
[49] M. M. Awad and R. A. Cheville, "Transmission terahertz waveguide-based imaging below the diffraction limit," *Applied Physics Letters,* vol. 86, p. 221107, 2005.
[50] W. Q. Zhu, A. Agrawal, and A. Nahata, "Planar plasmonic terahertz guided-wave devices," *Opt. Express,* vol. 16, pp. 6216-6226, 2008.
[51] R. Mendis, V. Astley, J. Liu, and D. M. Mittleman, "Terahertz microfluidic sensor based on a parallel-plate waveguide resonant cavity," *Applied Physics Letters,* vol. 95, p. 171113, 2009.
[52] V. Astley, K. S. Reichel, J. Jones, R. Mendis, and D. M. Mittleman, "Terahertz multichannel microfluidic sensor based on parallel-plate waveguide resonant cavities," *Applied Physics Letters,* vol. 100, p. 231108, 2012.
[53] R. Mendis and D. M. Mittleman, "Whispering-gallery-mode terahertz pulse propagation on a curved metallic plate," *Applied Physics Letters,* vol. 97, p. 031106, 2010.
[54] R. Mendis and D. M. Mittleman, "Multifaceted terahertz applications of parallel-plate waveguide: TE1 mode," *Electronics Letters,* vol. 46, pp. s40-s44, 2010.
[55] R. M. Marx Mbonye, and Daniel M. Mittleman, "Inhibiting the TE1 mode diffraction losses in terahertz parallel-plate waveguides using concave plates," *Optics Express,* 2012.
[56] R. Mendis and D. M. Mittleman, "A 2-D Artificial Dielectric With $0 < n < 1$ for the Terahertz Region," *Microwave Theory and Techniques, IEEE Transactions on,* vol. 58, pp. 1993-1998, 2010.
[57] J. Brown, "Artificial dielectrics having refractive indices less than unity," *Proceedings of the IEE - Part IV: Institution Monographs,* vol. 100, pp. 51-62, 1953.
[58] W. E. Kock, "Metal-Lens Antennas," *Proceedings of the IRE,* vol. 34, pp. 828-836, 1946.
[59] J. S. Seeley and J. Brown, "The use of dispersive artificial dielectrics in a beam-scanning prism," *Proceedings of the IEE - Part B: Radio and Electronic Engineering,* vol. 106, p. 93, 1959.
[60] W. Rotman, "Plasma simulation by artificial dielectrics and parallel-plate media," *Antennas and Propagation, IRE Transactions on,* vol. 10, pp. 82-95, 1962.
[61] A. Brown, Jr., "Pattern shaping with a metal plate lens," *Antennas and Propagation, IEEE Transactions on,* vol. 28, pp. 564-568, 1980.

[62] A. V. Kildishev, W. Cai, U. K. Chettiar, and V. M. Shalaev, "Transformation optics: approaching broadband electromagnetic cloaking," *New Journal of Physics,* vol. 10, p. 115029, 2008.
[63] J. Deibel, M. Escarra, N. Berndsen, K. Wang, and D. Mittleman, "Finite element method simulations of guided wave phenomena at terahertz frequencies," *Proc. IEEE,* vol. 95, pp. 1624-1640, 2007.
[64] B. Knoll and F. Keilmann, "Near-field probing of vibrational absorption for chemical microscopy," *Nature,* vol. 399, pp. 134-137, 1999.
[65] Q. Chen, Z. Jiang, G. X. Xu, and X. C. Zhang, "Near-field terahertz imaging with a dynamic aperture," *Opt. Lett.,* vol. 25, pp. 1122-1124, 2000.
[66] A. L. Bingham and D. Grischkowsky, "High Q, one-dimensional terahertz photonic waveguides," *Applied Physics Letters,* vol. 90, p. 091105, 2007.
[67] J. S. Melinger, S. S. Harsha, N. Laman, and D. Grischkowsky, "Guided-wave terahertz spectroscopy of molecular solids," *J. Opt. Soc. Am. B,* vol. 26, pp. A79-A89, 2009.
[68] J. S. Melinger, N. Laman, S. S. Harsha, S. Cheng, and D. Grischkowsky, "High-Resolution Waveguide Terahertz Spectroscopy of Partially Oriented Organic Polycrystalline Films," *The Journal of Physical Chemistry A,* vol. 111, pp. 10977-10987, 2007/11/01 2007.
[69] J. S. Melinger, N. Laman, S. S. Harsha, and D. Grischkowsky, "Line narrowing of terahertz vibrational modes for organic thin polycrystalline films within a parallel plate waveguide," *Applied Physics Letters,* vol. 89, p. 251110, 2006.
[70] A. Rusina, M. Durach, K. A. Nelson, and M. I. Stockman, "Nanoconcentration of terahertz radiation in plasmonic waveguides," *Opt. Express,* vol. 16, pp. 18576-18589, 2008.
[71] H. Zhan, R. Mendis, and D. M. Mittleman, "Superfocusing terahertz waves below ?/250 using plasmonic parallel-plate waveguides," *Opt. Express,* vol. 18, pp. 9643-9650, 2010.
[72] H. Zhan, R. Mendis, and D. M. Mittleman, "Characterization of the terahertz near-field output of parallel-plate waveguides," *J. Opt. Soc. Am. B,* vol. 28, pp. 558-566, 2011.
[73] M. Theuer, S. S. Harsha, and D. Grischkowsky, "Flare coupled metal parallel-plate waveguides for high resolution terahertz time-domain spectroscopy," *Journal of Applied Physics,* vol. 108, p. 113105, 2010.
[74] M. Theuer, A. J. Shutler, S. S. Harsha, R. Beigang, and D. Grischkowsky, "Terahertz two-cylinder waveguide coupler for transverse-magnetic and transverse-electric mode operation," *Applied Physics Letters,* vol. 98, p. 071108, 2011.
[75] M. Mbonye, R. Mendis, and D. M. Mittleman, "Study of the impedance mismatch at the output end of a THz parallel-plate waveguide," *Appl. Phys. Lett.,* vol. 100, p. 111120, 2012.

[76] J. Bae, T. Okamoto, T. Fujii, K. Mizuno, and T. Nozokido, "Experimental demonstration for scanning near-field optical microscopy using a metal micro-slit probe at millimeter wavelengths," *Applied Physics Letters,* vol. 71, pp. 3581-3583, 1997.
[77] T. Nozokido, N. Miyasaka, and J. Bae, "Near-field slit probe incorporating a micromachined silicon chip for millimeter-wave microscopy," *Microwave and Optical Technology Letters,* vol. 53, pp. 660-664, 2011.
[78] A. K. Jain, *Fundamentals of Digital Image Processing*. Englewood Cliffs, NJ: Prentice Hall, 1989.
[79] G. T. Herman, *Fundamentals of computerized tomography: Image reconstruction from projection*: 2nd edition, Springer, 2009.
[80] C. A. Balanis, *Advanced Engineering Electromagnetics*. New Jesey: Wiley, 1989.
[81] K. Iwaszczuk, A. Andryieuski, A. Lavrinenko, X.-C. Zhang, and P. U. Jepsen, "Non-invasive terahertz field imaging inside parallel plate waveguides," *Applied Physics Letters,* vol. 99, p. 071113, 2011.
[82] T. W. Ebbesen, H. J. Lezec, H. F. Ghaemi, T. Thio, and P. A. Wolff, "Extraordinary optical transmission through sub-wavelength hole arrays," *Nature,* vol. 391, pp. 667-669, 1998.
[83] T. Matsui, A. Agrawal, A. Nahata, and Z. V. Vardeny, "Transmission resonances through aperiodic arrays of subwavelength apertures," *Nature,* vol. 446, pp. 517-521, 2007.
[84] J. O'Hara, R. Averitt, and A. Taylor, "Prism coupling to terahertz surface plasmon polaritons," *Opt. Express,* vol. 13, pp. 6117-6126, 2005.
[85] T.-I. Jeon, J. Zhang, and D. Grischkowsky, "THz Sommerfeld wave propagation on a single metal wire," *Applied Physics Letters,* vol. 86, p. 161904, 2005.
[86] D. L. Mills and A. A. Maradudin, "Surface corrugation and surface-polariton binding in the infrared frequency range," *Physical Review B,* vol. 39, pp. 1569-1574, 1989.
[87] J. B. Pendry, L. Martin-Moreno, and F. J. Garcia-Vidal, "Mimicking surface plasmons with structured surfaces," *Science,* vol. 305, pp. 847-848, 2004.
[88] L. S. Mukina, M. M. Nazarov, and A. P. Shkurinov, "Propagation of THz plasmon pulse on corrugated and flat metal surface," *Surface Science,* vol. 600, pp. 4771-4776, 2006.
[89] B. G. Ghamsari and A. H. Majedi, "Terahertz transmission lines based on surface waves in plasmonic waveguides," *Journal of Applied Physics,* vol. 104, p. 083108, 2008.
[90] J. G. Rivas, M. Kuttge, P. H. Bolivar, H. Kurz, and J. A. Sánchez-Gil, "Propagation of Surface Plasmon Polaritons on Semiconductor Gratings," *Physical Review Letters,* vol. 93, p. 256804, 2004.
[91] F. J. Garcia-Vidal, L. Martín-Moreno, and J. B. Pendry, "Surfaces with holes in them: new plasmonic metamaterials

" *J. Opt. A: Pure Appl. Opt.,* vol. 7, pp. 97-101, 2005.
[92] C. R. Williams, S. R. Andrews, S. A. Maier, A. I. Fernandez-Dominguez, L. Martin-Moreno, and F. J. Garcia-Vidal, "Highly confined guiding of terahertz surface plasmon polaritons on structured metal surfaces," *Nat. Photon.,* vol. 2, pp. 175-179, 2008.
[93] N. Yu, J. Fan, Q. J. Wang, C. Pflügl, L. Diehl, T. Edamura, M. Yamanishi, H. Kan, and F. Capasso, "Small-divergence semiconductor lasers by plasmonic collimation," *Nat. Photon.,* vol. 2, pp. 564-570, 2008.
[94] N. Yu and F. Capasso, "Wavefront engineering for mid-infrared and terahertz quantum cascade lasers [Invited]," *J. Opt. Soc. Am. B,* vol. 27, pp. B18-B35, 2010.
[95] G. Veronis and F. Shanhui, "Modes of Subwavelength Plasmonic Slot Waveguides," *Lightwave Technology, Journal of,* vol. 25, pp. 2511-2521, 2007.
[96] D. F. P. Pile, T. Ogawa, D. K. Gramotnev, Y. Matsuzaki, K. C. Vernon, K. Yamaguchi, T. Okamoto, M. Haraguchi, and M. Fukui, "Two-dimensionally localized modes of a nanoscale gap plasmon waveguide," *Applied Physics Letters,* vol. 87, p. 261114, 2005.
[97] D. G. Cooke and P. U. Jepsen, "Optical modulation of terahertz pulses in a parallel plate waveguide," *Opt. Express,* vol. 16, pp. 15123-15129, 2008.
[98] H. E. M. Barlow, "Screened Surface Waves and Sows Possible. Applications," *Proc. IEEE,* vol. 112, p. 477, 1965.
[99] H. E. M. Barlow, " New Features of Wave Propogation Not Sub- ject to Cutoff Between Two Parallel Guiding Surfaces," *Proc. IEEE,* vol. 114, 1967.
[100] H. E. M. Barlow, "High-frequency wave propagation between parallel surfaces very close together " *J. Phys. D: Appl. Phys. ,* vol. 6, p. 929, 1973.
[101] V. Astley, H. Zhan, R. Mendis, and D. M. Mittleman, "A study of background signals in terahertz apertureless near-field microscopy and their use for scattering-probe imaging," *Journal of Applied Physics,* vol. 105, p. 113117, 2009.
[102] T. Rozzi and M. Mongiardo, *Open Electromagnetic Waveguides*, 1997.
[103] R. Yang, M. A. Abushagur, and Z. Lu, "Efficiently squeezing near infrared light into a 21nm-by-24nm nanospot," *Opt. Express,* vol. 16, pp. 20142-20148, 2008.
[104] M. A. Ordal, L. L. Long, R. J. Bell, S. E. Bell, R. R. Bell, J. R. W. Alexander, and C. A. Ward, "Optical properties of the metals Al, Co, Cu, Au, Fe, Pb, Ni, Pd, Pt, Ag, Ti, and W in the infrared and far infrared," *Appl. Opt.,* vol. 22, pp. 1099-1119, 1983.
[105] S. A. Maier, *Plasmonics: Fundamentals and Applications.* New York: Springer Science, 2007.
[106] Z. Fu, Q. Q. Gan, Y. J. Ding, and F. J. Bartoli, "From waveguiding to spatial localization of THz waves within a plasmonic metallic grating," *IEEE J. Sel. Top. Quant. Elec.,* vol. 14, pp. 486-490, 2008.

[107] J. Liu, R. Mendis, and D. M. Mittleman, "A tapered parallel-plate waveguide probe for THz near-field reflection imaging," *Appl. Phys. Lett.,* vol. 100, p. 031101, 2012.
[108] R. Mendis, "Guided-wave THz time-domain spectroscopy of highly doped silicon using parallel-plate waveguides," *Electronics Letters,* vol. 42, pp. 19-21, 2006.
[109] N. Laman, S. S. Harsha, D. Grischkowsky, and J. S. Melinger, "High-Resolution Waveguide THz Spectroscopy of Biological Molecules," *Biophysical journal,* vol. 94, pp. 1010-1020, 2008.
[110] S. A. Maier, *Plasmonics: Fundamentals and Applications*. New York: Springer Science+Business Media, 2007.
[111] J. Liu, R. Mendis, and D. M. Mittleman, "Designer reflectors using spoof surface plasmons in the terahertz range," *Phys. Rev. B,* vol. 86, p. 241405, 2012.
[112] S. A. Schelkunoff and H. T. Friis, *Antennas, Theory and Practice*. New York: Wiley, 1952.
[113] H. Poincare and F. K. Vreeland, *Maxwell's Theory and Wireless Telegraphy*. New York: McGraw, 1904.
[114] S. I. Bozhevolnyi, V. S. Volkov, E. Devaux, and T. W. Ebbesen, "Channel plasmon-polariton guiding by subwavelength metal grooves," *Phys. Rev. Lett.,* vol. 95, p. 046802, 2005.
[115] S. I. Bozhevolnyi, V. S. Volkov, E. Devaux, J.-Y. Laluet, and T. W. Ebbesen, "Channel plasmon subwavelength waveguide components including interferometers and ring resonators," *Nature,* vol. 440, pp. 508-511, 2006.
[116] C. Bonnet, D. Chauvat, O. Emile, F. Bretenaker, A. Le Floch, and L. Dutriaux, "Measurement of positive and negative Goos-Hänchen effects for metallic gratings near Wood anomalies," *Opt. Lett.,* vol. 26, pp. 666-668, 2001.
[117] X. Yin, L. Hesselink, Z. Liu, N. Fang, and X. Zhang, "Large positive and negative lateral optical beam displacements due to surface plasmon resonance," *Appl. Phys. Lett.,* vol. 85, pp. 372-374, 2004.
[118] M. Merano, A. Aiello, G. W. t' Hooft, M. P. van Exter, E. R. Eliel, and J. P. Woerdman, "Observation of Goos-Hänchen shifts in metallic reflection," *Opt. Express,* vol. 15, pp. 15928-15934, 2007.
[119] R. F. Gragg, "The total reflection of a compact wave group: Long-range transmission in a waveguide," *Am. J. Phys.,* vol. 56, pp. 1092-1094, 1988.
[120] M. Tonouchi, "Cutting-edge terahertz technology," *Nat Photon,* vol. 1, pp. 97-105, 2007.
[121] P. H. B. a. H. K. M Nagel, "Modular parallel-plate THz components for cost-efficient biosensing systems," *Semicond. Sci. Technol.,* vol. 20, pp. 281-285, 2005.
[122] B. B. Yang, S. L. Katz, K. J. Willis, M. J. Weber, I. Knezevic, S. C. Hagness, and J. H. Booske, "A High-Q Terahertz Resonator for the Measurement of Electronic

Properties of Conductors and Low-Loss Dielectrics," *Terahertz Science and Technology, IEEE Transactions on,* vol. 2, pp. 449-459, 2012.

[123] R. Braakman and G. A. Blake, "Principles and promise of Fabry--Perot resonators at terahertz frequencies," *Journal of Applied Physics,* vol. 109, p. 063102, 2011.

[124] Y. Chen, I. A. I. Al-Naib, J. Gu, M. Wang, T. Ozaki, R. Morandotti, and W. Zhang, "Membrane metamaterial resonators with a sharp resonance: A comprehensive study towards practical terahertz filters and sensors," *AIP Advances,* vol. 2, p. 022109, 2012.

[125] S. Preu, H. G. L. Schwefel, S. Malzer, G. H. Döhler, L. J. Wang, M. Hanson, J. D. Zimmerman, and A. C. Gossard, "Coupled whispering gallery moderesonators in the Terahertz frequency range," *Opt. Express,* vol. 16, pp. 7336-7343, 2008.

[126] P. A. George, C. Manolatou, F. Rana, A. L. Bingham, and D. R. Grischkowsky, "Integrated waveguide-coupled terahertz microcavity resonators," *Applied Physics Letters,* vol. 91, p. 191122, 2007.

[127] R. Mendis, V. Astley, J. Liu, and D. M. Mittleman, "Terahertz microfluidic sensor based on a parallel-plate waveguide resonant cavity," *Appl. Phys. Lett.,* vol. 95, p. 171113, 2009.

[128] M. Gerhard, C. Imhof, and R. Zengerle, "Compact three-dimensional terahertz resonators based on periodically corrugated metallic slit waveguides," *Journal of Applied Physics,* vol. 108, p. 026102, 2010.